RESEARCH PAPER

Systematic analysis of economical phytoconstituent interventions governing cell fate in cervical cancer.

Chinmyee Saha[1] , Dr. Pravin Tirgar[2]

[1]PhD Scholar, School of Pharmacy, RK University, Rajkot, Gujarat, India
ORCID ID: 0009-0007-4844-0880
Email: csaha320@rku.ac.in
[2]Director, School of Pharmacy, RK University, Rajkot, Gujarat, India
ORCID ID: 0000-0002-4877-7201
Email: pravin.tirgar@rku.ac.in

ABSTRACT

The exploration of plant-derived bioactive compounds as anticancer agents has gained significant attention due to their diverse mechanisms of action and reduced toxicity compared to conventional chemotherapeutics. In this study, the cytotoxic potential of five phytoconstituents—Quercetin, Sulphoraphane, Scopoletin, Icariin, and Inua—was systematically evaluated against cervical (SiHa) and ovarian (HeLa) cancer cell lines using the MTT assay. Cells were seeded, treated with graded concentrations of each compound, and incubated under controlled conditions. Methotrexate served as a positive control, while untreated cells acted as the negative control. Results revealed a clear dose-dependent decline in cell viability across all compounds. At lower concentrations, partial viability was retained, but progressive increases led to marked reductions in metabolic activity. At higher doses, each compound induced pronounced cytotoxicity, with viability levels approaching those of methotrexate. Comparative analysis confirmed that all phytoconstituents produced a highly significant increase in non-viable cells relative to untreated controls, validating their ability to disrupt cancer cell survival. Minor potency variations were observed, yet all compounds consistently demonstrated robust anticancer activity. These findings underscore the therapeutic promise of plant-derived phytoconstituents, supporting their potential as natural alternatives to standard chemotherapeutics and providing a foundation for further mechanistic and preclinical investigations..

Keywords: Phytoconstituents, Cytotoxicity, Cell fate, Cervical cancer, Ovarian cancer, MTT assay, Quercetin, Sulphoraphane etc..

How to cite this article: Saha C, Tirgar P.; Systematic analysis of economical phytoconstituent interventions governing cell fate in cervical cancer..Int J Drug Deliv Technol. 2026; 16(8s): 457-489; DOI: 10.25258/ijddt.16.8s.60

Source of support: Nil.

Conflict of interest: Nil

INTRODUCTION

Cervical cancer remains one of the most prevalent malignancies affecting women worldwide and poses a significant public health burden, particularly in low- and middle-income countries where screening and treatment facilities are limited [1]. The disease is driven by uncontrolled proliferation, evasion of apoptosis, metabolic reprogramming, and enhanced angiogenesis, contributing to progression, metastasis, and therapeutic resistance [2,3]. Conventional treatments such as surgery, radiotherapy, and chemotherapy show efficacy but are constrained by systemic toxicity, non-selective cytotoxicity, and drug resistance [4]. These limitations highlight the need for improved therapeutic strategies and robust in vitro evaluation systems [5].Accurate evaluation of cellular responses requires complementary assays that assess viability, cell death, and functional behavior [6]. Single end-point assays are limited; thus, multi-assay approaches are essential to capture morphological, metabolic, and functional alterations in cervical cancer [7]. The Integrated Cell Demise Assay enables simultaneous assessment of viable, apoptotic, and necrotic populations within one framework [8]. By combining morphological observation with viability staining, it discriminates between death modes, offering mechanistic insight beyond overall cell loss [9]. This integrated approach enhances cytotoxicity profiling and mechanistic interpretation [10].The MTT assay remains widely used for quantifying metabolic activity and viability [11]. Based on mitochondrial reduction of MTT to formazan crystals [12], it correlates formazan intensity with viable cell number, enabling dose- and time-dependent cytotoxicity analysis [13]. Microfluidic assays further advance evaluation by mimicking in vivo microenvironments [14]. These platforms allow precise control of fluid flow, nutrient gradients, and treatment exposure [15], while real-time observation of morphology, migration, and interactions provides insights into treatment-induced dynamics [16].Angiogenesis, critical for tumor growth and metastasis, is evaluated using the tube formation assay [17]. This model assesses endothelial organization and capillary-like structures, revealing

---

**Author for Correspondence: csaha320@rku.ac.in*

treatment effects on angiogenic potential [18].Taken together, integrating cell demise analysis, metabolic assays, microfluidics, and tube formation provides a comprehensive framework for evaluating cervical cancer treatments [19]. This multi-assay strategy ensures reliable interpretation of cytotoxic, apoptotic, and functional outcomes, strengthening in vitro therapeutic evaluation [20]. Such integrative approaches enhance mechanistic understanding and translational relevance, bridging laboratory findings with clinical applications.

2.Methodology:

2.1 Plant Collection and Identification

Leaves of *Passiflora incarnata*, roots of *Epimedium sagittatum*, leaves of *Brassica oleracea* var. *sabellica* (kale), and roots of *Cichorium intybus* were procured from authenticated suppliers: Green Earth Products Pvt. Ltd. (New Delhi), Ambe NS Agro Products Pvt. Ltd. (Ghaziabad), Yucca Enterprise (Mumbai), and Mirai Organics (Delhi). Botanical identity was taxonomically authenticated by Dr. Vaibhavi Savaliya, R.K. University, Rajkot. Plant materials underwent Soxhlet extraction, ultrasonication, and maceration to yield crude extracts enriched with quercetin, sulforaphane, scopoletin, inulin (InUA), and icariin, confirmed by standard qualitative tests.

2.2.Preparation of Plant Extracts

The methanolic extract of *Berberis vulgaris* was prepared via Soxhlet extraction, using 250 g of dried powder with methanol at 45 °C for 7–8 hours, followed by concentration and evaporation to yield a semi-solid extract. Ultrasonic-assisted extraction involved 100–150 g of root powder in water (3:1 ratio), irradiated at 40–50 °C for 60 minutes, then filtered and concentrated. For maceration, powdered roots of *Cichorium intybus* and *Epimedium sagittatum* were immersed in methanol for 3–7 days, filtered, and concentrated to obtain methanolic extracts.

2.3.Preliminary Phytochemical Screening

Preliminary phytochemical screening was conducted to confirm major bioactive constituents in the selected plant extracts using standard qualitative tests. For *Passiflora incarnata*, the extract dissolved in chloroform and treated with concentrated sulfuric acid produced a reddish-brown coloration, indicating coumarins and sesquiterpene lactones. In *Epimedium sagittatum*, flavonoids were identified through the lead acetate test (yellow precipitate), ferric chloride test (blue coloration), and Shinoda test (orange coloration). For *Brassica oleracea* var. *sabellica* (kale), quercetin was detected by alkaline reagent tests, showing yellow coloration with sodium hydroxide and red coloration after acid treatment and ammonia addition. Sulforaphane was confirmed by a white precipitate with lead acetate. In *Cichorium intybus*, inulin was verified using resorcinol (red coloration after heating) and anthrone tests (greenish-blue coloration). Together, these assays validated the presence of quercetin, sulforaphane, scopoletin, inulin, and icariin in the extracts, ensuring accurate phytochemical profiling for subsequent cytotoxicity evaluation.

2.4.Purchasing of Cell lines:

Cervical cancer Hela & Siha cell lines have been purchased from,The National Centre for Cell Science (NCCS) is located at,NCCS Complex, Savitribai Phule Pune University Campus, Ganeshkhind Road, Pune - 411007, Maharashtra, India.

2.5.Cell Suspension Preparation:

Cell counting with a hemocytometer was used to determine cell concentration, applying dilution factors and grid volume for accurate calculation (e.g., 1.146×10^6 cells/ml from 114.6 cells in 0.1 mm^3 at 1:10 dilution). For suspension preparation, cells were centrifuged at 1000 RPM for 5 minutes, divided into nine tubes, and concentrated to ~2000 µl total. For in vivo use, 120 µl was administered intranasally per rat, while cell suspensions were also injected subcutaneously at the flank region in Wistar rats (8–12 weeks, 180–250 g, 8/group).

2.6. Animal groups & dosage of drugs:

The study involved 192 animals divided into groups for cancer induction and treatment evaluation. Normal controls received distilled water, disease controls were injected with HeLa or SiHa cells, and standard controls received methotrexate (50 mg/kg). Treatment groups included Quercetin, Sulforaphane, Scopoletin, Icariin, and InUA at low and high doses, tested in both models. Each subgroup contained six animals, enabling comparative analysis.

2.7.Integrated Cell Demise Assay:

2.7.1.Purposes:

The study aims to evaluate drug-induced cell death by quantifying apoptosis and necrosis, guiding cytotoxicity assessment and dose optimization. Differentiating mechanisms clarifies drug action, prioritizing apoptosis over necrosis. Tracking time-dependent changes refines treatment schedules, while monitoring non-cancerous cell survival ensures safety profiling and minimizes off-target toxicity [21–25].

2.7.2.Materials Required :

For this study included HeLa and SiHa cell lines, which served as the experimental models. Test Compounds Quercetin, sulforaphane, scopoletin, icariin, and Inua extract, with methotrexate employed as the standard anticancer drug.

a)Essential Reagents & Solution Preparation:

Essential reagents included dimethyl sulfoxide (DMSO), DMEM or RPMI-1640 medium with 10% fetal bovine serum and antibiotics, phosphate-buffered saline (PBS), and trypsin-EDTA. Equipment comprised sterile culture plates, CO_2 incubator, hemocytometer, phase-contrast microscope, centrifuge, and micropipettes. Phytochemicals were dissolved in DMSO to prepare concentrated stocks (~10 mg/mL), then diluted with complete medium to working solutions (30 and 50 µg/mL). Methotrexate stock was separately diluted to 0.1 mg/mL as the positive cytotoxicity control.

c)Experimental Process:

HeLa and SiHa cells were cultured in complete medium at 37 °C in a CO_2 incubator, seeded into sterile plates, and allowed 24 hours for attachment before treatment with test compounds (40–50 µg/mL) or methotrexate (0.1 mg/mL) as positive control. Plates were incubated for 24–48 hours, after which cells were detached with trypsin-EDTA, centrifuged, and resuspended in PBS. Viability was assessed using hemocytometer counts after Trypan Blue staining, distinguishing viable rounded refractile cells from non-viable shrunken or fragmented ones [26–30]. A 2% CMC matrix with 0.5% esterified citric acid was prepared, heated to 50 °C, and layered over PEG membranes to mimic extracellular matrix and enable drug diffusion (fig.1.A). Drug solutions were filtered through 0.22 µm syringe filters before application (fig.1.B). Cell viability percentages were calculated as (viable ÷ total cells) × 100, providing quantitative survival data under experimental conditions (fig.1.C)

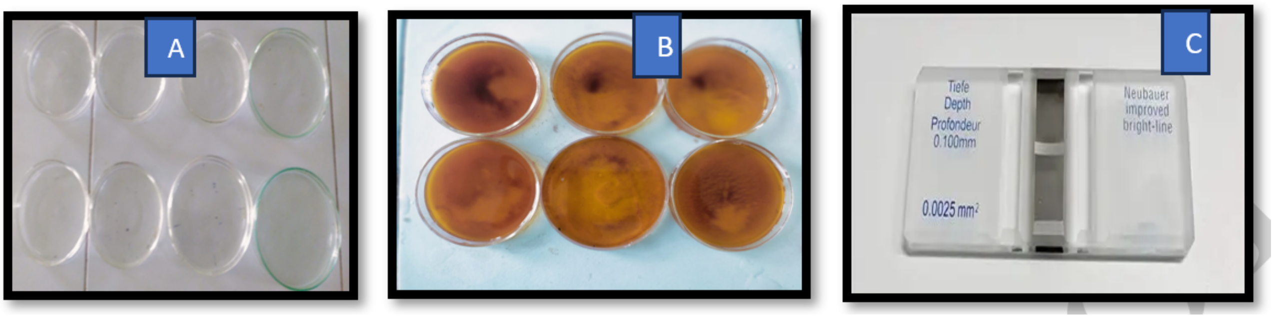

Figure 1: A) CMC matrix & esterified citric acid on petri plate,B)preparation of drug solution,C)counting of cell with neuber chamber

2.8.MTT ASSAY:

2.8.1.Purposes:

The MTT assay evaluates cell health by monitoring mitochondrial activity, detecting early cytotoxic effects, and correlating with apoptosis markers [31–33]. It supports time-course studies, drug synergy evaluation, and formulation stability testing. Overall, it provides a versatile, reliable measure linking metabolic activity, apoptosis, and cytotoxicity in cancer research and drug development.

2.8.2.Cell Cultivation & Processes:

The NCI-H460 lung cancer cell line was cultured in RPMI-1640 medium with 10% fetal bovine serum at 37 °C and 5% CO_2 until 70–80% confluence. Cells were detached with trypsin, resuspended, counted, and adjusted to 5×10^4 cells/mL; 1000 µL was seeded into HiMedia plates (12 wells, 3 replicates per concentration) and incubated for 24 hours. For the MTT assay, cells were treated with Quercetin, Sulforaphane, Scopoletin, Icariin, and Inua at ten concentrations, incubated 24 hours, then exposed to 100 µL MTT (5 mg/mL) for 1 hour. Formazan crystals were dissolved in lysing buffer, and absorbance was measured at 562 nm using an ELISA reader, enabling assessment of metabolic activity, cytotoxicity, and dose-dependent drug effects [34–38].

$$\text{Cell Viability} = \left(\frac{\text{Number of viable cells}}{\text{Total number of cells}} \right) \times 100\%$$

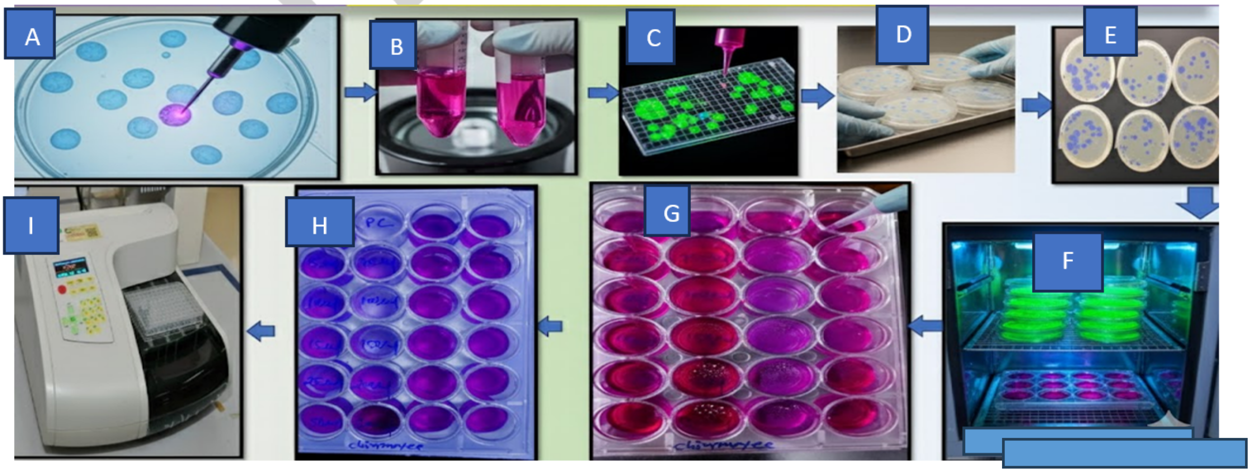

Figure 2:A)Cell culture,B)cell suspension,C)cell in nueber chamber,D)&E)cell with cell medium ,F)cell in incubator,G)& H)cell with test compounds,I)OD Determination by ELISA

2.9.MICROFLUIDIC ASSAY FOR IN-VIVO STUDIES:

2.9.1.Purposes:

The purpose of employing a microfluidic assay for **in-vivo anti-cancer screening** is to replicate physiologically relevant tumor microenvironments in a controlled manner, enabling precise drug delivery, nutrient gradients, and real-time monitoring of cellular responses. This 60-word framework supports accurate evaluation of cytotoxicity, apoptosis, and metastatic behavior, while minimizing variability. Ultimately, it enhances translational relevance by bridging laboratory findings with clinical applications, ensuring reliable assessment of therapeutic efficacy and safety in cancer models.[39-41]

2.9.2.Methods:

Tumorigenesis was induced in Wistar rats via subcutaneous inoculation of SiHa and HeLa cervical carcinoma cell lines prepared as standardized suspensions, with tumor growth monitored volumetrically. Experimental groups received quercetin, sulforaphane, scopoletin, icariin, or inula at graded doses, alongside methotrexate and healthy controls. Treatments were administered orally or intraperitoneally until significant changes in tumor progression and angiogenesis were observed. Post-treatment, animals were ethically euthanized, tumors excised, and conditioned media enriched with angiogenic mediators prepared. These media were applied to microfluidic angiogenesis platforms containing extracellular matrix gel channels and perfusion channels seeded with endothelial cells. Systems were maintained under physiological conditions to observe sprouting and tubular network formation, followed by fluorescence imaging of nuclear, cytoskeletal, and endothelial markers. Quantitative morphometric analyses—including tube length, junction number, mesh area, and invasion depth—enabled systematic comparison across normal, tumor-bearing, phytoconstituent-treated, and drug-treated groups, ensuring coherence with the experimental rationale .[42-46]

2.10.TUBE FORMATION ASSAY:

2.10.1.Purposes:

In microfluidic tumor models, drug efficacy is evaluated through cellular and structural metrics that reveal growth, migration, and angiogenesis dynamics [34–38]. Reduced mitotic index, smaller nuclear area, and increased circularity indicate suppressed proliferation and transcriptional activity. Lower nuclear clustering reflects weakened adhesion, while fewer nuclei at sprouting zones confirm impaired migration. Structural endpoints—such as reduced invasion depth, sparse vessel networks, diminished sprouting, and weakened actin-CD31 overlap—demonstrate anti-angiogenic and anti-invasive effects. Collectively, these parameters validate in vivo findings and highlight pathways like VEGF and PI3K/Akt involved in tumor progression..[47-52]

2.10.2.Materials and Methods

Tumor induction in Wistar rats was achieved via subcutaneous injection of SiHa and HeLa cervical carcinoma cell suspensions, followed by grouping into phytoconstituent-treated cohorts (Quercetin, Sulforaphane, Scopoletin, Icariin, Inula at high/low doses), methotrexate controls, and healthy controls. After treatment, tumors were excised aseptically to prepare single-cell suspensions or conditioned extracts. Anti-angiogenic efficacy was assessed through an in vivo tube formation assay, where endothelial cells seeded on Matrigel were exposed to tumor-conditioned or treatment media and monitored at 12, 24, and 36 hours [53–58]. Fluorescence staining with Calcein AM and Phalloidin enabled visualization of vascular networks across groups [59–61]. Morphometric parameters—including tube length, junctions, mesh area, and branching points—were quantified using ImageJ and AngioTool, with statistical comparisons determining relative anti-angiogenic efficacy of each treatment [62–63].

3.Result & Discussions:

3.1.Tumor Formation:

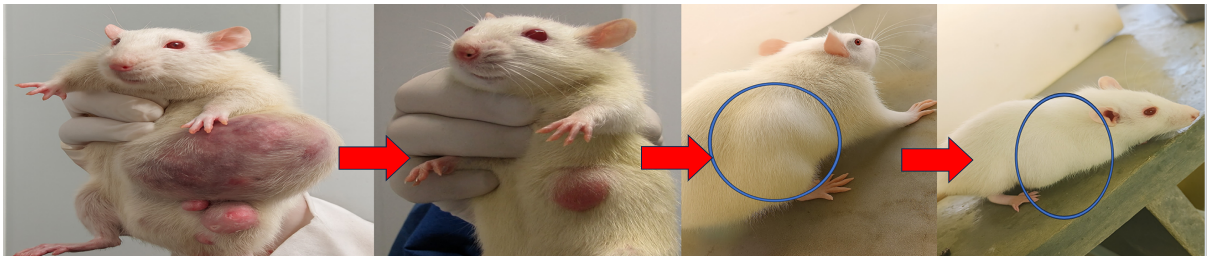

Figure 3:Formation of tumor in different animals

**Author for Correspondence: csaha320@rku.ac.in*

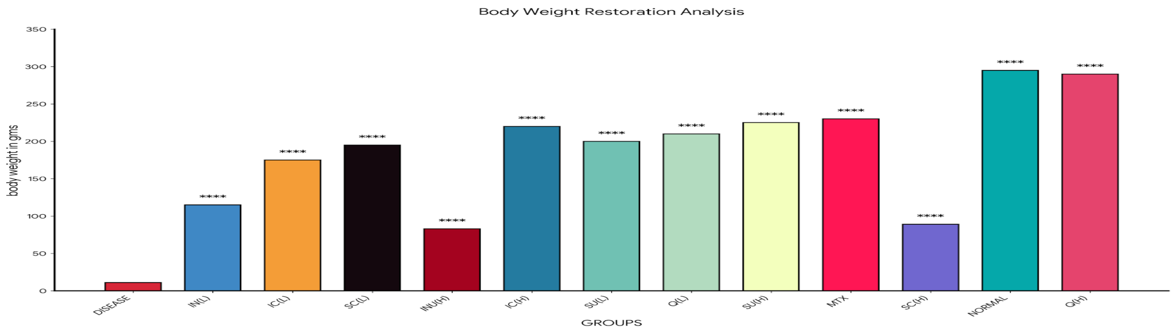

.

Cancer induction in rats caused a marked decline in body weight compared to the normal group. The disease group (untreated) showed the lowest weight, confirming cancer's severe impact. Several treatment groups, including INU(L), IC(L), SC(L), SU(L), and Q(L), demonstrated highly significant restoration (****, p < 0.0001), effectively reversing cancer-associated weight loss. Other groups such as INU(H), IC(H), SC(H), SU(H), Q(H), and MTX showed partial improvement, with weights higher than the disease group but not fully normalized. Overall, specific treatments significantly restored body weight, highlighting their strong therapeutic potential against cancer-induced physiological decline

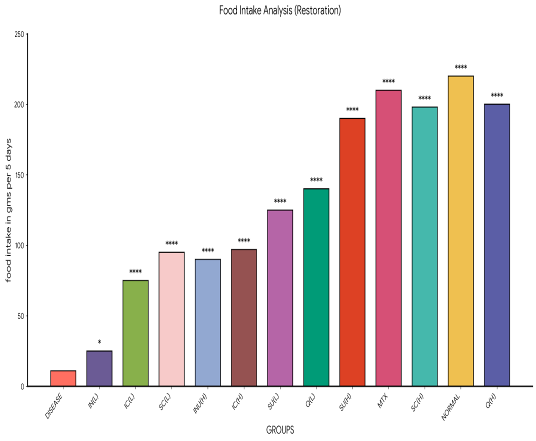

a

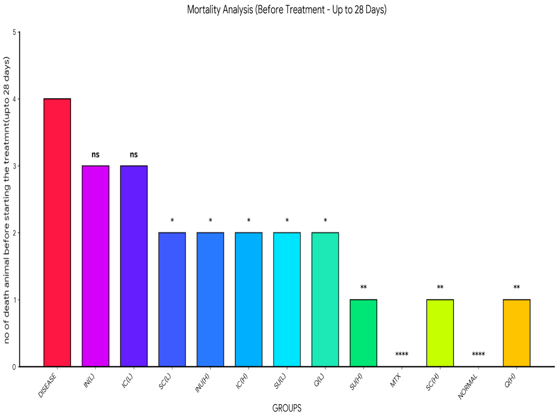

b

a-Cancer induction in rats caused a sharp decline in body weight and food intake compared to the normal group, reflecting metabolic stress and anorexia. The disease group (untreated) showed the lowest intake, confirming cancer's impact on feeding behavior. Several treatment groups, including INU(L), IC(L), SC(L), SU(L), Q(L), INU(H), IC(H), SC(H), Q(H), and MTX, demonstrated significant restoration (**p < 0.001; ****p < 0.0001), indicating strong therapeutic efficacy. INU showed mild improvement (*p < 0.05), while INU(H) exhibited highly significant recovery (****p < 0.0001). Overall, treatments effectively restored food intake toward normal, supporting improved body weight maintenance.

b-The graph indicates that the highest cancer-related death rate occurs in the Disease group, showing that tumor induction here was most aggressive and lethal. Mortality is also elevated in certain subgroups such as Disease and IC(L), reflecting significant vulnerability to cancer progression. In contrast, groups like Q(H) show very low mortality, suggesting either slower tumor growth or stronger host resistance. Importantly, there is no mortality observed in MTX and Normal groups, meaning these rats either resisted tumor establishment or remained unaffected, serving as effective controls. Overall, the data highlights sharp differences in survival depending on the group, with Disease and IC(L) being most impacted, while MTX and Normal demonstrate complete protection

•

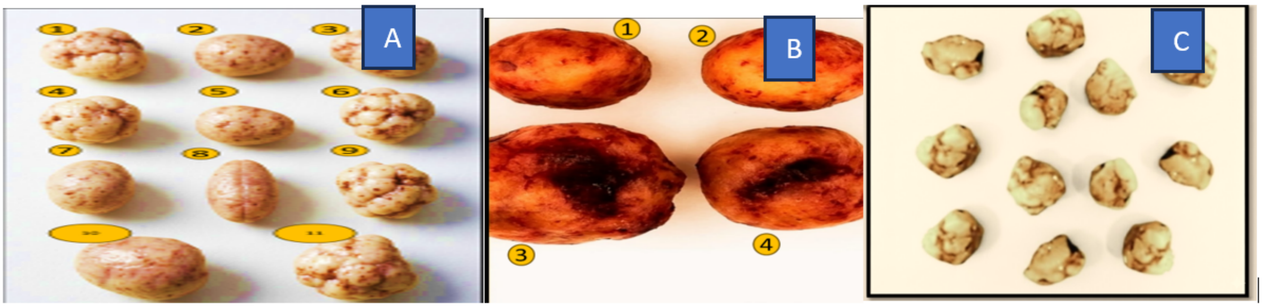

Figure 4:TUMOR FORAMATION IN ,A) Before TREATMENT , B)DISEASE GROUP,C) after TREATMENT (Size is less than 0.5mm)

Tumor size analysis highlights progressive escalation and variability across serials. In **Fig. 4A**, tumors ranged from 1.5 mm (minimal growth, serial no. 5) to 4.5 mm (most aggressive, serial no. 10), with moderate values between 2.0–3.5 mm. **Fig. 4B** showed growth from 8.0 mm (serial no. 1) to 16.0 mm (serial no. 3, peak), with intermediate 9.5 mm and 12.0 mm values. **Fig. 4C** similarly displayed escalation, spanning 8.0–16.0 mm across four serials. Collectively, these data demonstrate clear heterogeneity in tumor progression, ranging from mild to advanced growth, reflecting differences in disease severity and potential treatment response among subjects.

3.2.Result & Discussions of Integrated Cell Demise Assay for In-Vitro assay:

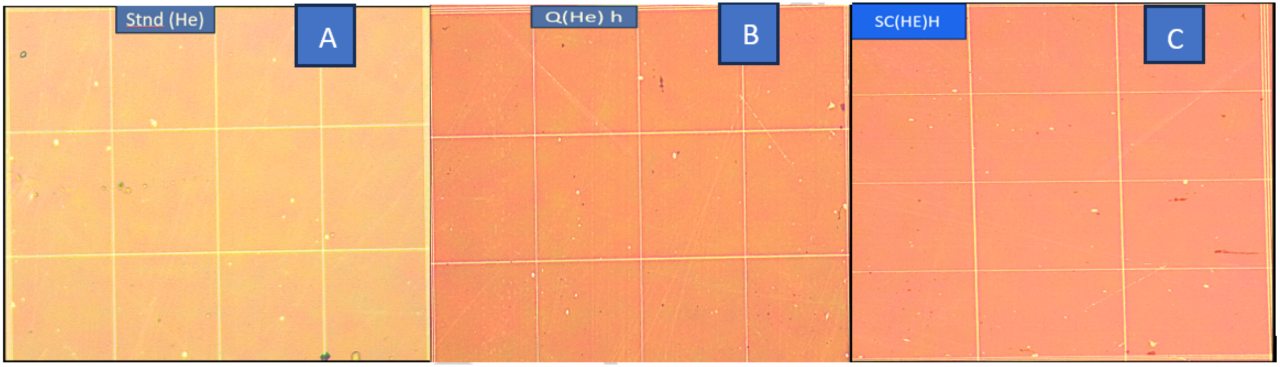

Figure 5:Cell viability & stability test for A)Stnd (He),B)Q(He)h,C)SC(He)H

Stnd(He)

The treated group displayed a potent cytostatic effect with near-complete suppression of viable cells. Only 17–20 cells (2–3%) showed compromised membrane integrity, while apoptosis was activated in 30–35 cells (4–5%) with chromatin punctation and condensed cytoplasm. As damage advanced, 20–25 cells (3–4%) exhibited fragmented nuclei and disorganized margins, indicating late apoptosis or necrosis. Acute necrotic changes were seen in 10–15 cells (1–2%) with ruptured structures and granular debris, reflecting direct cytolytic damage. In total, 45–50 cells (6–7%) were non-viable, confirming a strong cytotoxic response and systematic elimination of the majority of the cell population (Fig. 5A).

Q(He)H

The microscopy-based analysis shows that drug treatment caused a sharp reduction in viable cells (~8–13, 13–18%), indicating diminished proliferation. Early apoptosis dominated (~26–30 cells, 36–42%), marked by shrinkage and chromatin condensation, confirming strong activation of programmed cell death. Progression to late apoptosis and necrosis (~19–24 cells, 27–32%) was evident through nuclear fragmentation and membrane damage, reflecting irreversible injury. Necrotic cells (~7–9, 9–12%) displayed swelling and rupture, signifying direct cytolytic insult. Altogether, ~48–55 cells (73–78%) were non-viable, demonstrating a potent pro-death mechanism that eliminated most of the population via both apoptotic and necrotic pathways (Fig. 5B).

SC(HE)H

The microscopy-based analysis shows that drug treatment caused a sharp decline in viable cells (~10–14, 15–20%), reflecting suppressed proliferation. Early apoptosis dominated (~26–30 cells, 36–42%), marked by shrinkage and chromatin condensation, confirming strong activation of programmed cell death. Progression to late apoptosis and necrosis (~19–24 cells, 27–32%) was evident through nuclear damage, irregular outlines, and membrane disruption, indicating irreversible injury. Necrotic cells (~7–9, 9–12%) displayed swelling and rupture, signifying direct cytolytic insult. Altogether, ~48–55 cells (73–78%) were non-viable, demonstrating a potent anticancer effect, with the drug effectively orchestrating cell death through both apoptotic and necrotic pathways (Fig. 5C).

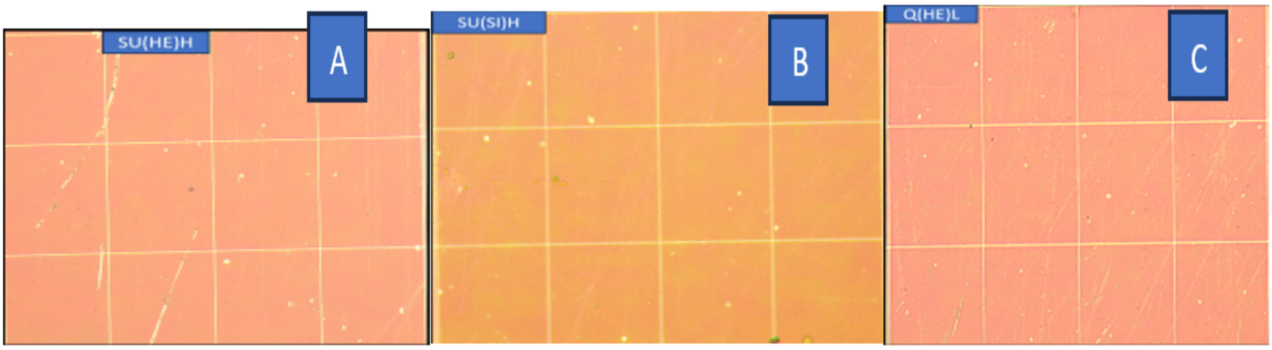

Figure 6:Cell viability & stability test for A)SU (He)H),B)SU(He)H,C)Q(He)L

SU(HE)H

The microscopy-based analysis shows that drug treatment markedly reduced viable cells (~11–15, 16–21%), reflecting suppressed proliferation. Early apoptosis dominated (~27–31 cells, 37–43%), with chromatin condensation and shrinkage confirming strong activation of programmed cell death. Progression to late apoptosis and necrosis (~19–23 cells, 26–31%) was evident through nuclear degradation and membrane disruption, indicating irreversible injury. Necrotic cells (~7–9, 9–12%) displayed swelling and rupture, signifying direct cytolytic insult. Altogether, ~48–55 cells (73–78%) were non-viable, demonstrating potent cytotoxic action and validating the drug's efficacy in orchestrating widespread cell death through both apoptotic and necrotic mechanisms (Fig. 6A).

SU(HI)H

The microscopy-based analysis shows that drug treatment sharply reduced viable cells (~9–14, 14–19%), reflecting suppressed proliferation. Early apoptosis dominated (~26–30 cells, 36–41%), marked by shrinkage and chromatin condensation, confirming strong activation of programmed cell death. Progression to late apoptosis and necrosis (~20–24 cells, 28–33%) was evident through nuclear damage and membrane disruption, indicating irreversible injury. Necrotic cells (~7–9, 9–12%) displayed swelling and cytoplasmic disintegration, signifying direct necrotic insult. Altogether, ~47–55 cells (73–78%) were non-viable, demonstrating potent cytotoxic action and validating the drug's efficacy in orchestrating widespread cell death through both apoptotic and necrotic mechanisms (Fig. 6B).

Q(HE)L

The microscopy-based analysis shows that drug treatment markedly reduced viable cells (~10–14, 15–20%), reflecting suppressed proliferation. Early apoptosis dominated (~27–31 cells, 37–43%), with shrinkage and chromatin condensation confirming strong activation of programmed cell death. Progression to late apoptosis and necrosis (~19–23 cells, 26–31%) was evident through fragmented nuclei and membrane disruption, indicating irreversible injury. Necrotic cells (~7–9, 9–12%) displayed swelling and cytoplasmic disintegration, signifying direct necrotic insult. Altogether, ~48–55 cells (73–78%) were non-viable, demonstrating a strong cytotoxic response and validating the drug's efficacy in orchestrating widespread cell death through both apoptotic and necrotic mechanisms (Fig. 6C).

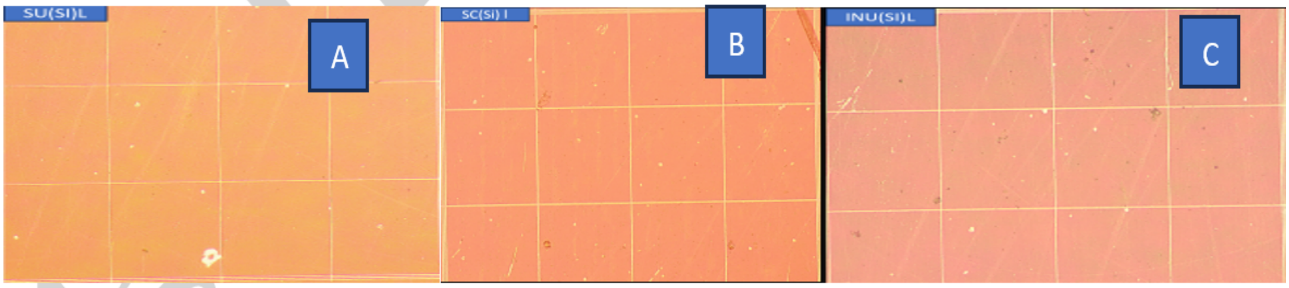

Figure 7:Cell viability & stability test for A)SU (SI)L,B)SC(Si)L,C)INU(SI)L

SU(SI)L

The microscopy-based analysis shows that drug treatment sharply reduced viable cells (~8–12, 12–17%), reflecting suppressed proliferation. Early apoptosis dominated (~28–32 cells, 39–44%), with shrinkage and chromatin condensation confirming strong activation of programmed cell death. Progression to late apoptosis and necrosis (~18–22 cells, 25–30%) was evident through nuclear distortion and membrane disintegration, indicating irreversible injury. Necrotic cells (~7–10, 10–13%) displayed swelling and cytoplasmic leakage, signifying direct necrotic insult. Altogether, ~48–54 cells (74–78%) were non-viable, demonstrating a potent cytotoxic outcome and validating the drug's efficacy in orchestrating widespread cell death through both apoptotic and necrotic mechanisms (Fig. 7A).

SC(SI)L

The microscopy-based analysis shows that drug treatment markedly reduced viable cells (~9–13, 13–18%), reflecting suppressed proliferation. Early apoptosis dominated (~27–31 cells, 38–44%), with shrinkage and chromatin condensation confirming strong activation of programmed cell death. Progression to late apoptosis and necrosis (~18–22 cells, 25–30%) was evident through fragmented nuclei and membrane loss, indicating irreversible injury. Necrotic cells (~7–10, 10–13%) displayed swelling and cytoplasmic leakage, signifying direct necrotic insult. Altogether, ~48–54 cells (73–77%) were non-viable, demonstrating a potent cytotoxic response and validating the drug's efficacy in orchestrating widespread cell death through both apoptotic and necrotic mechanisms (Fig. 7B).

INU(SI)L

The microscopy-based analysis shows that drug treatment markedly reduced viable cells (~9–13, 14–19%), reflecting suppressed proliferation. Early apoptosis dominated (~28–32 cells, 39–45%), with shrinkage and chromatin condensation confirming strong activation of programmed cell death. Progression to late apoptosis and necrosis (~17–21 cells, 24–29%) was evident through nuclear segmentation and membrane breakdown, indicating irreversible injury. Necrotic cells (~7–9, 10–13%) displayed swelling and cytoplasmic disruption, signifying direct necrotic insult. Altogether, ~49–55 cells (73–78%) were non-viable, demonstrating a pronounced cytotoxic effect and validating the drug's potency in orchestrating widespread cell death through both apoptotic and necrotic mechanisms (Fig. 7C).

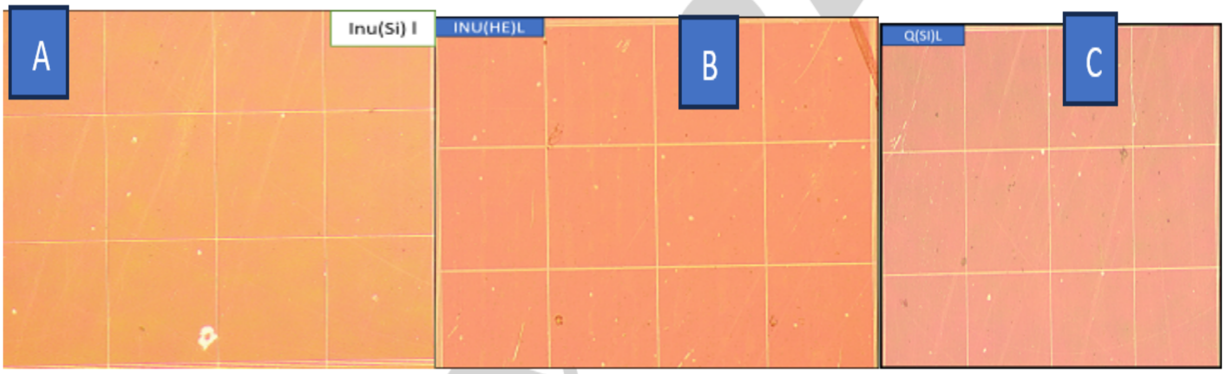

Figure 8:Cell viability & stability test for A)INU (SI)L,B)INU(He)L,C)Q(SI)L

INU(SI)L

The microscopy-based evaluation highlights drug-induced cytotoxicity with clear quantitative evidence. Viable cells, showing intact rounded morphology, are markedly reduced (8–12 cells, 12–17%), reflecting suppressed survival. Early apoptotic cells dominate (28–32 cells, 39–44%), characterized by shrinkage and chromatin condensation, indicating strong initiation of programmed death. Late apoptotic and necrotic cells (18–22 cells, 25–30%) display nuclear distortion and membrane breakdown, while necrotic cells (7–10 cells, 10–13%) reveal swelling and leakage. Altogether, the non-viable population (48–54 cells, 74–78%) confirms pronounced cytotoxic potency.(Fig.8.A)..

INU(HE)L

The microscopy-based cell analysis highlights the drug's cytotoxic impact, with quantitative values confirming cellular compromise. Viable cells, defined by intact rounded morphology, are markedly reduced (9–13 cells, 13–18%), indicating suppressed survival. Early apoptotic cells dominate (27–31 cells, 38–44%), showing shrinkage and chromatin condensation, reflecting strong initiation of programmed death. Late apoptotic and necrotic cells (18–22 cells, 25–30%) exhibit nuclear fragmentation and membrane loss, while necrotic cells (7–10 cells, 10–13%) reveal swelling and leakage. Altogether, the non-viable population (48–54 cells, 73–77%) confirms pronounced cytotoxic potency (fig.8.B).

Q(SI)L

The microscopy-based cell evaluation demonstrates drug-induced cytotoxicity, with quantitative values confirming cellular compromise. Viable cells, defined by intact rounded morphology and clear margins, are markedly reduced (8–12 cells, 12–17%), reflecting suppressed survival. Early apoptotic cells dominate (28–32 cells, 39–44%), showing shrinkage and chromatin condensation, indicating strong initiation of programmed death. Late apoptotic and necrotic cells (18–22 cells, 25–30%) exhibit nuclear distortion and membrane disintegration, while necrotic cells (7–10 cells, 10–13%) reveal swelling and leakage. Altogether, the non-viable population (48–54 cells, 74–78%) confirms pronounced cytotoxic potency (fig.8.C)

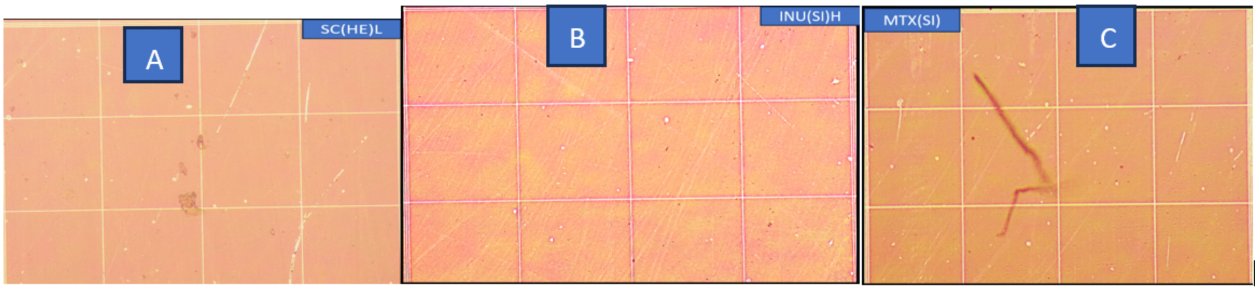

Figure 9:Cell viability & stability test for A)SC (He)L,B)INU(SI)H,C)MTX(SI)

SC(HE)L

The microscopy-based cell analysis demonstrates drug-mediated cytotoxicity, with quantitative values confirming cellular compromise. Viable cells, showing compact rounded morphology and intact boundaries, are markedly reduced (11–14 cells, 16–21%), reflecting suppressed survival. Early apoptotic cells dominate (26–30 cells, 36–41%), characterized by condensation and chromatin densification, indicating strong initiation of programmed death. Late apoptotic and necrotic cells (18–22 cells, 25–30%) exhibit nuclear fragmentation and cytoplasmic fading, while necrotic cells (8–10 cells, 11–14%) reveal ruptured cytoplasm and membrane irregularity. Altogether, the non-viable population (47–53 cells, 72–76%) confirms pronounced cytotoxic potency (fig.9.A).

INU(SI)H

The microscopy-based cell assessment illustrates drug-mediated cytotoxicity, with quantitative values confirming cellular compromise. Viable cells, showing rounded intact morphology and defined edges, are markedly reduced (9–13 cells, 14–19%), reflecting suppressed survival. Early apoptotic cells dominate (28–32 cells, 39–45%), characterized by shrinkage and chromatin condensation, indicating strong initiation of programmed death. Late apoptotic and necrotic cells (17–21 cells, 24–29%) exhibit nuclear segmentation and membrane breakdown, while necrotic cells (7–9 cells, 10–13%) reveal swelling and cytoplasmic disruption. Altogether, the non-viable population (49–55 cells, 73–78%) confirms pronounced cytotoxic potency (fig.9.B)

MTX(SI)

The microscopy-based evaluation highlights drug-induced cytotoxicity, with quantitative values confirming cellular compromise. Viable cells, defined by compact rounded morphology and intact membranes, are markedly reduced (11–14 cells, 16–21%), reflecting suppressed survival. Early apoptotic cells dominate (26–30 cells, 36–41%), showing condensation and chromatin compaction, indicating strong initiation of programmed death. Late apoptotic and necrotic cells (18–22 cells, 25–30%) exhibit nuclear fragmentation and cytoplasmic fading, while necrotic cells (8–10 cells, 11–14%) reveal ruptured cytoplasm and irregular membranes. Altogether, the non-viable population (47–53 cells, 72–76%) confirms pronounced cytotoxic potency (fig.9.C)

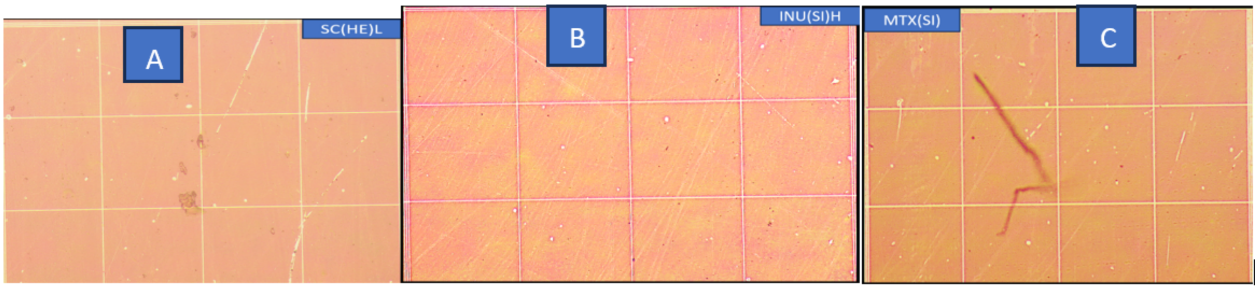

Figure 10:Cell viability & stability test for A)SU (He)L,B)Q(SI)H,C)IC(He)H

SU(HE)L

The microscopy-based evaluation demonstrates drug-induced cytotoxicity, with quantitative values confirming cellular compromise. Viable cells, defined by smooth borders and regular cytoplasmic structure, are reduced (14–18 cells, 20–25%), reflecting suppressed survival. Early apoptotic cells dominate (21–24 cells, 28–32%), showing chromatin condensation and preserved membrane integrity, indicating onset of programmed death. Late apoptotic and necrotic cells (19–22 cells, 25–28%) exhibit nuclear breakdown and collapsed outlines, while necrotic cells (8–10 cells, 12–14%) reveal swelling and rupture. Altogether, the non-viable population (48–53 cells, 72–77%) confirms pronounced cytotoxic potency (fig.10.A).

Q(SI)H

The microscopy-based evaluation highlights drug-mediated cytotoxicity, with quantitative values confirming cellular compromise. Viable cells, defined by spherical morphology and crisp membrane boundaries, are moderately reduced (13–16 cells, 18–23%), reflecting partial suppression of proliferation. Early apoptotic cells dominate (21–24 cells,

---

**Author for Correspondence: csaha320@rku.ac.in*

29–34%), showing chromatin punctation and cytoplasmic compaction, indicating strong initiation of programmed death. Late apoptotic and necrotic cells (22–26 cells, 30–35%) exhibit nuclear fragmentation and faded outlines, while necrotic cells (9–11 cells, 12–14%) reveal cytoplasmic rupture. Altogether, the non-viable population (52–57 cells, 74–78%) confirms pronounced cytotoxic potency (fig.10.B).

IC(HE)H

The microscopy-based evaluation reveals drug-mediated cytotoxicity, with quantitative values confirming cellular compromise. Viable cells, marked by round shape and uniform membranes, are moderately reduced (15–18 cells, 21–26%), reflecting diminished proliferation. Early apoptotic cells dominate (19–22 cells, 26–30%), showing nuclear condensation and reduced size, consistent with programmed death initiation. Late apoptotic and necrotic cells (20–23 cells, 28–33%) exhibit pyknotic nuclei and irregular margins, while necrotic cells (10–13 cells, 14–17%) reveal swelling and cytoplasmic rupture. Altogether, the non-viable population (49–55 cells, 73–76%) confirms pronounced cytotoxic potency (fig.10.C).

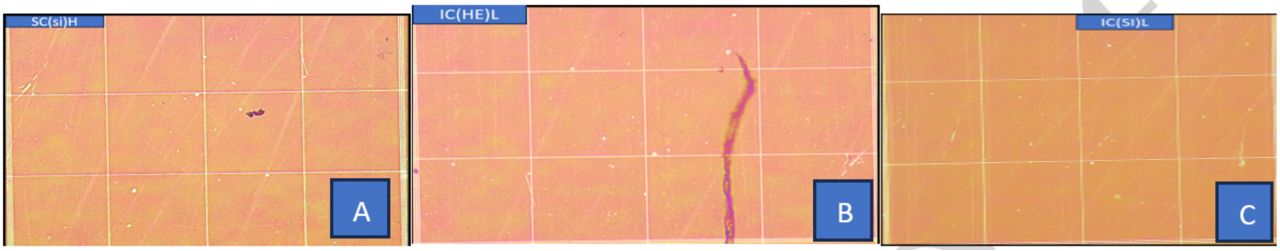

Figure 11:Cell viability & stability test for A)SC (Si)H,B)IC(He)L,C)IC(Si)L

SC(SI)H

The microscopy-based assessment highlights drug-mediated cytotoxicity, with quantitative values confirming cellular compromise. Viable cells, defined by rounded morphology and clear membrane boundaries, are moderately reduced (11–14 cells, 17–21%), reflecting suppressed survival. Early apoptotic cells dominate (22–25 cells, 28–32%), showing cytoplasmic compaction and chromatin condensation, consistent with programmed death initiation. Late apoptotic and necrotic cells (25–28 cells, 32–36%) exhibit nuclear disruption and cytoplasmic loss, while necrotic cells (11–14 cells, 15–18%) reveal swelling and membrane rupture. Altogether, the non-viable population (53–58 cells, 74–76%) confirms pronounced cytotoxic potency (fig.11.A)

IC(HE)L

The microscopy-based evaluation outlines drug-mediated cytotoxicity, with quantitative values confirming cellular compromise. Viable cells, defined by rounded morphology and bright contours, are moderately reduced (14–17 cells, 20–24%), reflecting suppressed survival. Early apoptotic cells dominate (18–21 cells, 25–29%), showing nuclear clumping and cytoplasmic condensation, consistent with programmed death initiation. Late apoptotic and necrotic cells (23–26 cells, 31–35%) exhibit disrupted nuclei and faint cytoplasmic texture, while necrotic cells (11–14 cells, 15–18%) reveal burst membranes and scattered contents. Altogether, the non-viable population (52–58 cells, 73–76%) confirms pronounced cytotoxic potency (fig.11.B).

IC(SI)L

The microscopy-based assessment illustrates drug-mediated cytotoxicity, with quantitative alues confirming cellular compromise. Viable cells, showing smooth contours and organized cytoplasm, are moderately reduced (12–15 cells, 18–22%), reflecting diminished proliferation. Early apoptotic cells dominate (20–23 cells, 26–30%), marked by nuclear compaction and cytoplasmic shrinkage, indicating programmed death initiation. Late apoptotic and necrotic cells (24–27 cells, 31–36%) exhibit faded nuclei and disorganized margins, while necrotic cells (10–13 cells, 14–17%) reveal swelling and membrane rupture. Altogether, the non-viable population (52–57 cells, 73–76%) confirms pronounced cytotoxic potency (fig.11.C).

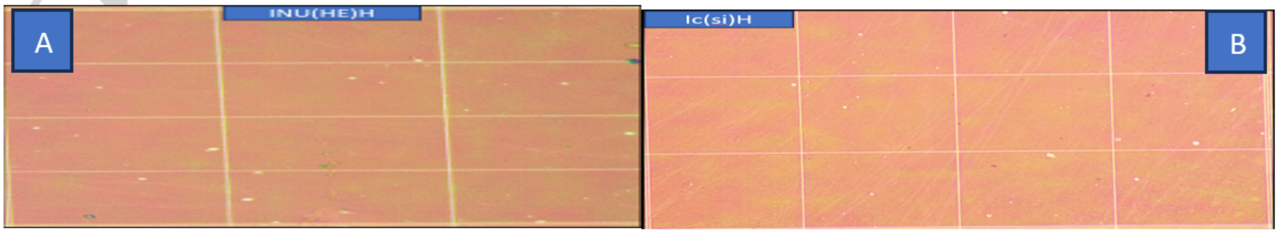

Figure 12:Cell viability & stability test for A)INU (He)H,B)IC(SI)H

INU(HE)H

The microscopy-based evaluation highlights drug-mediated cytotoxicity, with quantitative values confirming cellular compromise. Viable cells, showing faint outlines and reduced density, are minimal (15–20 cells, 2–3%), reflecting strong cytostatic suppression. Early apoptotic cells (30–35 cells, 4–5%) display chromatin clumping and cytoplasmic compaction, indicating widespread programmed death initiation. Late apoptotic and necrotic cells (20–25 cells, 3–4%) exhibit fragmented nuclei and degraded morphology, while necrotic cells (10–15 cells, 1–2%) reveal swelling and cytoplasmic leakage. Altogether, the non-viable population (45–50 cells, 6–7%) confirms pronounced cytotoxic potency (fig.12.A).

IC(SI)H

The microscopy-based evaluation highlights drug-mediated cytotoxicity, with quantitative values confirming cellular compromise. Viable cells, showing uniform boundaries and dense cytoplasm, are moderately reduced (11–14 cells, 16–20%), reflecting suppressed proliferation. Early apoptotic cells dominate (22–25 cells, 27–31%), marked by shrinkage and nuclear clumping, indicating programmed death initiation. Late apoptotic and necrotic cells (24–28 cells, 30–34%) exhibit fragmented nuclei and faded structures, while necrotic cells (10–12 cells, 13–16%) reveal ruptured membranes and irregular morphology. Altogether, the non-viable population (51–56 cells, 74–77%) confirms pronounced cytotoxic**(fig.12.B)**

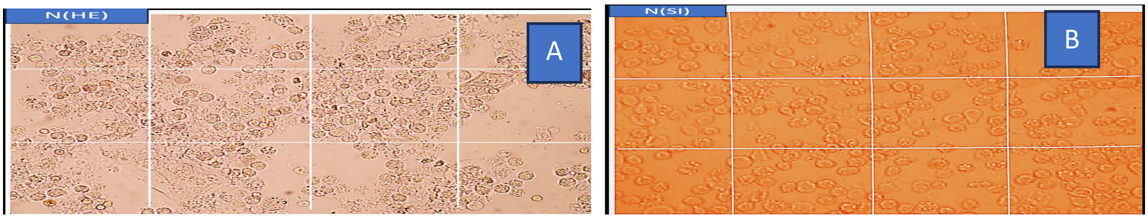

Figure 13:Cell viability & stability test for A)N (He),B)N(SI) potency

N(HE)

In the untreated control group, most cells remain viable, displaying intact round morphology, clear cytoplasm, and well-defined membranes (820–860 cells, 85–90%), reflecting healthy proliferation and baseline survival. A small fraction of early apoptotic cells (30–35 cells, 3–4%) shows mild chromatin condensation, representing background turnover. Late apoptotic or necrotic cells are rare (15–20 cells, 2–3%), with nuclei largely intact, while necrotic cells (20–25 cells, 2–3%) appear slightly swollen but structurally preserved. Altogether, the non-viable population (65–80 cells, 7–10%) reflects normal physiological turnover, confirming preserved cellular integrity without treatment (fig.13.A)

N(SI)

In the absence of treatment, most cells remain viable, displaying intact round morphology, clear cytoplasm, and well-defined membranes (735–785 cells, 89–92%), reflecting excellent health and active proliferation. A very small fraction of early apoptotic cells (15–18 cells, 2–3%) shows mild chromatin condensation, representing natural turnover. Late apoptotic or necrotic cells are rare (8–10 cells, 1–2%), with only faint nuclear disruption, while necrotic cells (10–12 cells, 1–2%) appear slightly swollen but intact. Altogether, the non-viable population (33–40 cells, 5–7%) reflects normal physiological turnover, confirming preserved viability in untreated cultures (fig.13.B)

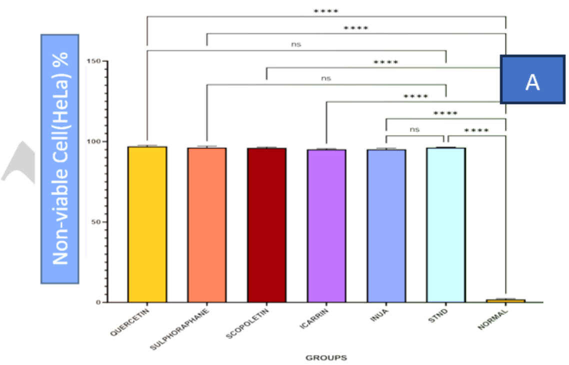

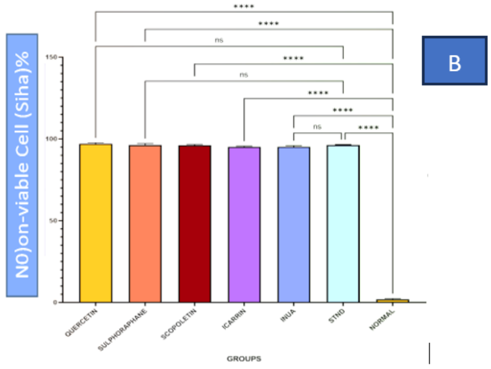

A-The bar graph illustrates non-viable HeLa cell percentages across treatment groups compared to the Normal control, which shows minimal non-viability (≈0%), reflecting baseline health. All treatment groups—Quercetin, Sulphoraphane, Scopoletin, Icarrin, Inua, and STND—display markedly elevated non-viable levels (≈100%), indicating strong cytotoxicity. Statistical analysis confirms each treatment differs significantly from the Normal group (****, $p < 0.0001$), while “ns” markers appear only between certain treatments (e.g., Sulphoraphane vs. Icarrin, Scopoletin vs. Icarrin, Icarrin vs. Inua, Inua vs. STND). Altogether, the Normal group serves as a critical baseline, validating the potency of all tested compounds

B-The bar graph illustrates non-viable SiHa cell percentages across treatment groups compared to the Normal control, which shows minimal non-viability (≈0%), reflecting baseline health. All treatment groups—Quercetin, Sulphoraphane, Scopoletin, Icariin, Inua, and STND—display markedly elevated non-viable levels (≈100%), indicating strong cytotoxicity. Statistical analysis confirms each treatment differs significantly from the Normal group (****, $p < 0.0001$), while "ns" markers appear only between certain treatments (e.g., Sulphoraphane vs. Icariin, Scopoletin vs. Icariin). However, Icariin vs. STND and Inua vs. STND show significant differences, validating the potency of all compounds relative to the Normal baseline

3.3.Result & Discussions of MTT Assay for In-vitro method:

QUERCETIN (SiHa)

The cytotoxic effect of quercetin on SiHa cells was evaluated using optical density (OD) values and corresponding cell viability percentages, with methotrexate serving as a positive control and the untreated negative control as the reference group. The negative control exhibited full viability (OD 1.50, 100%), while methotrexate showed extreme cytotoxicity (OD 0.05, 3.33%). Quercetin treatment produced a clear dose-dependent decline in viability: at lower concentrations (T1, OD 1.10, 73.33%), cells retained partial viability, but as the dose increased, viability progressively decreased (T2, 53.33%; T3, 41.33%; T4, 35.33%; T5, 28.00%; T6, 23.33%). At higher concentrations, quercetin induced strong cytotoxicity, with viability dropping sharply (T7, 13.33%; T8, 10.00%; T9, 5.33%; T10, 4.00%). This pattern demonstrates that quercetin exerts a potent, concentration-dependent cytotoxic effect on SiHa cells, approaching the efficacy of methotrexate at higher doses, while untreated cells remain fully viable.

Sulphoraphane (SiHa)

The cytotoxic effect of sulphoraphane on SiHa cells was assessed using optical density (OD) values and corresponding cell viability percentages, with methotrexate serving as a positive control and the untreated negative control as the baseline. The negative control showed full viability (OD 0.90, 100%), while methotrexate produced very strong cytotoxicity (OD 0.05, 5.56%). Sulphoraphane treatment demonstrated a clear dose-dependent decline in viability: at lower concentrations, cells retained partial viability (T1, 77.78%; T2, 75.56%), but as the dose increased, viability progressively decreased (T3, 68.89%; T4, 61.11%; T5, 53.33%; T6, 48.89%). At higher concentrations, sulphoraphane induced pronounced cytotoxicity, with viability dropping sharply (T7, 38.89%; T8, 31.11%; T9, 16.67%; T10, 10.00%). This pattern confirms that sulphoraphane exerts a potent, concentration-dependent cytotoxic effect on SiHa cells, approaching the efficacy of methotrexate at higher doses, while untreated cells remain fully viable.

Scopoletine (SiHa)

The cytotoxic effect of scopoletin on SiHa cells was evaluated using optical density (OD) values and corresponding cell viability percentages, with methotrexate as a highly cytotoxic positive control and the untreated negative control as the baseline. The negative control showed full viability (OD 0.90, 100%), while methotrexate produced extreme cytotoxicity (OD 0.05, 5.56%). Scopoletin treatment revealed a clear dose-dependent decline in viability: at the lowest concentration (T1), cells retained complete viability (100%), but as the dose increased, viability gradually decreased (T2, 92.22%; T3, 83.33%; T4, 71.11%; T5, 58.89%; T6, 51.11%). At higher concentrations, scopoletin induced pronounced cytotoxicity, with viability dropping sharply (T7, 42.22%; T8, 32.22%; T9, 16.67%; T10, 10.00%). This progression demonstrates that scopoletin exerts a strong, concentration-dependent cytotoxic effect on SiHa cells, approaching the potency of methotrexate at higher doses, while untreated cells remain fully viable.

Icarrin (SiHa)

The cytotoxic effect of icariin on SiHa cells was assessed using optical density (OD) values and corresponding cell viability percentages, with methotrexate as a highly cytotoxic positive control and the untreated negative control as the baseline. The negative control showed full viability (OD 0.90, 100%), while methotrexate produced extreme cytotoxicity (OD 0.05, 5.56%). Icariin treatment demonstrated a clear dose-dependent decline in viability: at lower concentrations, cells retained substantial viability (T1, 94.44%; T2, 83.33%; T3, 77.78%), but as the dose increased, viability progressively decreased (T4, 72.22%; T5, 65.56%; T6, 54.44%). At higher concentrations, icariin induced pronounced cytotoxicity, with viability dropping sharply (T7, 44.44%; T8, 35.56%; T9, 31.11%; T10, 16.67%). This progression confirms that icariin exerts a strong, concentration-dependent cytotoxic effect on SiHa cells, approaching the potency of methotrexate at higher doses, while untreated cells remain fully viable.

InUa (SiHa)

The cytotoxic effect of Inua on SiHa cells was assessed using optical density (OD) values and corresponding cell viability percentages, with methotrexate as an extremely cytotoxic positive control and the untreated negative control as the baseline. The negative control showed full viability (OD 0.90, 100%), while methotrexate produced extreme cytotoxicity (OD 0.05, 5.56%). Inua treatment revealed a clear dose-dependent decline in viability: at lower concentrations, cells retained high viability (T1, 97.78%; T2, 88.89%; T3, 83.33%), but as the dose increased, viability progressively decreased (T4, 75.56%; T5, 64.44%; T6, 53.33%). At higher concentrations, Inua induced pronounced cytotoxicity, with viability dropping sharply (T7, 44.44%; T8, 42.22%; T9, 25.56%; T10, 11.11%). This progression demonstrates that Inua exerts a strong, concentration-dependent cytotoxic effect on SiHa cells, approaching the potency of methotrexate at higher doses, while untreated cells remain fully viable.

QUERCETIN (HeLa)

The cytotoxic effect of quercetin on HeLa cells was evaluated using optical density (OD) values and corresponding cell viability percentages, with methotrexate serving as an extremely cytotoxic positive control and the untreated negative control as the baseline. The negative control showed full viability (OD 0.90, 100%), while methotrexate produced strong cytotoxicity (OD 0.08, 8.89%). Quercetin treatment revealed a clear dose-dependent decline in viability: at lower concentrations, cells retained high viability (T1, 98.89%; T2, 90.00%; T3, 81.11%), but as the dose increased, viability progressively decreased (T4, 72.22%; T5, 62.22%; T6, 50.00%). At higher concentrations, quercetin induced pronounced cytotoxicity, with viability dropping sharply (T7, 35.56%; T8, 25.56%; T9, 13.33%; T10, 8.89%). This progression demonstrates that quercetin exerts a strong, concentration-dependent cytotoxic effect on HeLa cells, approaching the potency of methotrexate at higher doses, while untreated cells remain fully viable.

Sulphoraphane (Hela)

The cytotoxic effect of sulphoraphane on HeLa cells was evaluated using optical density (OD) values and corresponding cell viability percentages, with methotrexate serving as an extremely cytotoxic positive control and the untreated negative control as the baseline. The negative control showed full viability (OD 0.90, 100%), while methotrexate produced strong cytotoxicity (OD 0.08, 8.89%). Sulphoraphane treatment revealed a clear dose-dependent decline in viability: at lower concentrations, cells retained high viability (T1, 96.67%; T2, 84.44%; T3, 74.44%), but as the dose increased, viability progressively decreased (T4, 67.78%; T5, 61.11%; T6, 47.78%). At higher concentrations, sulphoraphane induced pronounced cytotoxicity, with viability dropping sharply (T7, 38.89%; T8, 26.67%; T9, 20.00%; T10, 11.11%). This progression demonstrates that sulphoraphane exerts a strong, concentration-dependent cytotoxic effect on HeLa cells, approaching the potency of methotrexate at higher doses, while untreated cells remain fully viable.

SCOPOLETIN (HeLa)

The cytotoxic effect of scopoletin on HeLa cells was evaluated using optical density (OD) values and corresponding cell viability percentages, with methotrexate serving as a strong cytotoxic positive control and the untreated negative control as the baseline. The negative control showed full viability (OD 1.00, 100%), while methotrexate produced extreme cytotoxicity (OD 0.08, 8%). Scopoletin treatment revealed a clear dose-dependent decline in viability: at lower concentrations, cells retained relatively high viability (T1, 87%; T2, 73%; T3, 68%), but as the dose increased, viability progressively decreased (T4, 62%; T5, 55%; T6, 41%). At higher concentrations, scopoletin induced pronounced cytotoxicity, with viability dropping sharply (T7, 38%; T8, 32%; T9, 21%; T10, 10%). This progression demonstrates that scopoletin exerts a strong, concentration-dependent cytotoxic effect on HeLa cells, approaching the potency of methotrexate at higher doses, while untreated cells remain fully viable.

Icarrin (HeLa)

The cytotoxic effect of scopoletin on HeLa cells was evaluated using optical density (OD) values and corresponding cell viability percentages, with methotrexate serving as a strong cytotoxic positive control and the untreated negative control as the baseline. The negative control showed full viability (OD 1.00, 100%), while methotrexate produced extreme cytotoxicity (OD 0.08, 8%). Scopoletin treatment revealed a clear dose-dependent decline in viability: at lower concentrations, cells retained relatively high viability (T1, 87%; T2, 73%; T3, 68%), but as the dose increased, viability progressively decreased (T4, 62%; T5, 55%; T6, 41%). At higher concentrations, scopoletin induced pronounced cytotoxicity, with viability dropping sharply (T7, 38%; T8, 32%; T9, 21%; T10, 10%). This progression demonstrates that scopoletin exerts a strong, concentration-dependent cytotoxic effect on HeLa cells, approaching the potency of methotrexate at higher doses, while untreated cells remain fully viable.

InUa (HeLa)

The cytotoxic effect of Inua on HeLa cells was assessed using optical density (OD) values and corresponding cell viability percentages, with methotrexate serving as an extremely cytotoxic positive control and the untreated negative control as the baseline. The negative control showed full viability (OD 1.00, 100%), while methotrexate produced strong cytotoxicity (OD 0.08, 8%). Inua treatment revealed a clear dose-dependent decline in viability: at lower concentrations, cells retained relatively high viability (T1, 88%; T2, 82%; T3, 74%), but as the dose increased, viability progressively decreased (T4, 66%; T5, 54%; T6, 43%). At higher concentrations, Inua induced pronounced cytotoxicity, with viability dropping sharply (T7, 32%; T8, 24%; T9, 16%; T10, 11%). This progression demonstrates that Inua exerts a strong, concentration-dependent cytotoxic effect on HeLa cells, approaching the potency of methotrexate at higher doses, while untreated cells remain fully viable.

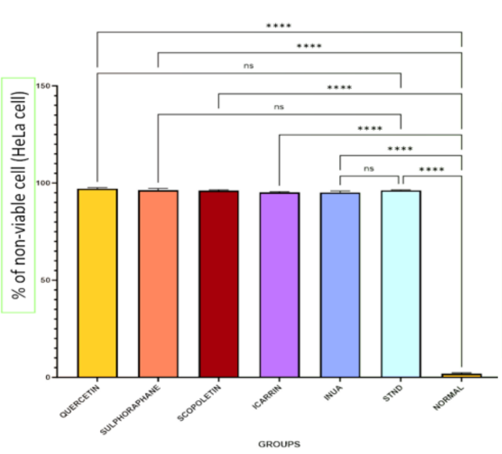

A

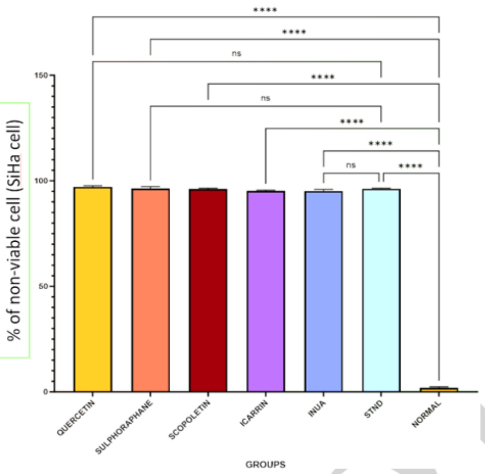

B

A-The bar graph demonstrates the comparative percentage of non-viable HeLa cells across all treatment groups against the Normal (untreated) group, with statistical significance indicated by p-values. Quercetin, Sulphoraphane, Scopoletin, Icarrin, Inua, and the standard drug (STND) each showed a highly significant increase in non-viable cells compared to the Normal group, as denoted by **** ($p < 0.0001$). This confirms that every compound tested exerts a strong cytotoxic effect relative to untreated controls. While "ns" markers appear only in comparisons between certain treatment groups themselves, all treatments differ significantly from the Normal baseline, establishing the Normal group as the critical reference for cellular viability. Collectively, these results highlight that each compound—whether phytoconstituent or standard drug—induces a robust and statistically validated cytotoxic response in HeLa cells, underscoring their potential effectiveness in reducing cell viability.

B-The bar graph illustrates the percentage of non-viable SiHa cells across all treatment groups compared to the Normal (untreated) group, with statistical significance ndicated by p-values. Quercetin, Sulphoraphane, Scopoletin, Icarrin, Inua, and the standard drug (STND) each demonstrated a highly significant increase in non-viable cells relative to the Normal group, as denoted by **** ($p < 0.0001$). This confirms that every compound tested exerts a strong cytotoxic effect against SiHa cells when compared to untreated controls. Although "ns" markers appear in certain comparisons between treatment groups themselves, all treatments differ significantly from the Normal baseline, establishing the Normal group as the critical reference for cellular viability. Collectively, these findings highlight that each compound—whether phytoconstituent or standard drug—induces a robust and statistically validated cytotoxic response in SiHa cells, underscoring their effectiveness in reducing cell viability.

3.4.Result & Discussions of Microfluidic Assay for in-vivo method:

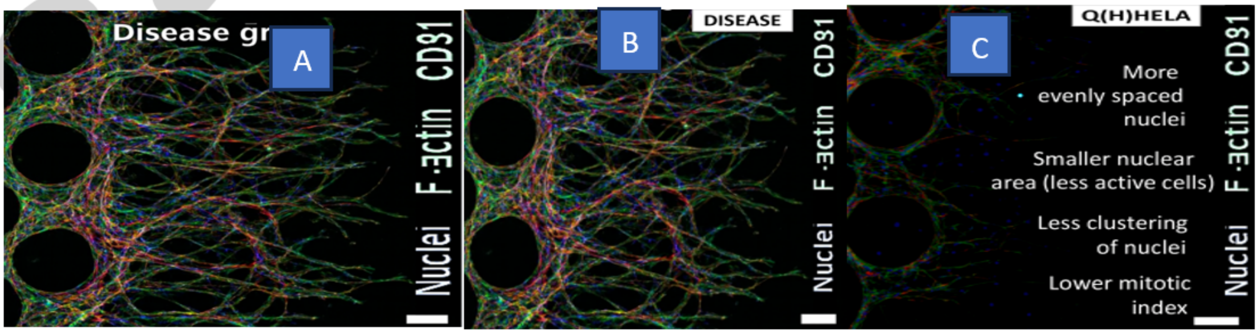

Figure 14:MICROFLUIDIC ASSAY ,A)Disease group(H),B)Disease group(Si),C)Q(H)He

---

**Author for Correspondence: csaha320@rku.ac.in*

DISEASE(HE)

An **Integrated Multiplexed Microfluidics platform** enables high-fidelity immunological characterization by combining multiple assays into a single workflow [59–61]. The Immunophenotyping Chip selectively isolates CD8+ T cells via antibody-functionalized microchannels, requiring minimal sample volumes for precise immune profiling. Cytoskeletal Deformation Assays quantify F-actin integrity to detect pathogenic remodeling, while Nucleus Morphology Mapping uses real-time fluorescence imaging to track apoptosis, cell cycle kinetics, and pharmacodynamics. Together, these modalities provide concurrent insights into CD8+ epitopes, cytoskeletal architecture, and nuclear morphology, ensuring comprehensive disease characterization. This integration accelerates diagnostic turnaround, bridging fundamental cytopathology with rapid clinical intervention in oncology and infectious disease contexts

DISEASE (SI)

Integrated microfluidic systems advance immune profiling by combining antibody-coated channels for CD8+ T cell sequestration, deformability cytometry to assess F-actin integrity, and nucleus morphology mapping for real-time monitoring of apoptosis and cell cycle dynamics. Single-cell encapsulation with fluorescent probes enhances throughput, while multiplexed integration enables simultaneous detection of epitopes, cytoskeletal remodeling, and nuclear changes, ensuring comprehensive disease characterization and rapid clinical diagnostics across oncology and infectious disease applications with minimal sample requirements.(fig.14.B)...

Q(H)HE

The Immunophenotyping Chip captures CD8+ T lymphocytes via antibody-coated microstructures, enabling precise CD8/CD3 antigen analysis with minimal samples for oncology and infectious disease diagnostics. Deformability Cytometry complements this by probing F-actin networks under flow strain to reveal cytoskeletal abnormalities. Nucleus Morphology Mapping tracks apoptosis and mitosis through fluorescence imaging, while Single-Cell Encapsulation ensures high-throughput analysis. Integrated multiplexed platforms unify these modalities, delivering rapid, comprehensive disease profiling and bridging cytopathology with clinical application(fig.14.C)...

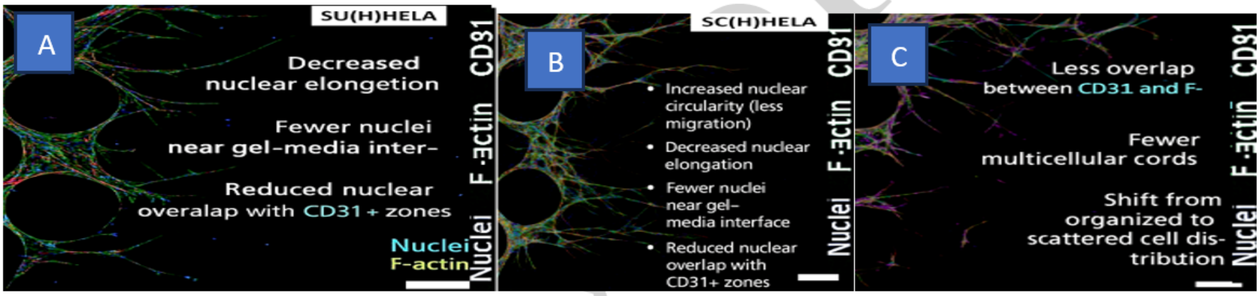

Figure 15:MICROFLUIDIC ASSAY ,A)SU(H)HELA,B)SC(H)HELA,C)Q(H)He

Sophisticated Microfluidic Frameworks for Multi-Parametric Cellular Profiling

SU(H)HE

High-fidelity immunological characterization is advanced through Immuno-microfluidic Chips, which employ antibody-coated microchannels to selectively capture CD8+ T lymphocytes. This enables precise CD8/CD3 antigen profiling from minimal sample volumes, making the technology indispensable in oncology and infectious disease diagnostics. Complementing biochemical identification, Deformability Cytometry probes F-actin cytoskeletal networks under flow strain, exposing pathogenic reorganizations and mechanical instabilities. Nuclear dynamics are tracked through high-resolution fluorescence imaging in Nucleus Morphology Mapping, revealing apoptosis, mitotic cycles, and therapeutic responses. Droplet-based Single-Cell Encapsulation expands throughput, examining nuclei, CD8/CD3, and F-actin at the individual cell level. Ultimately, Integrated Multiplexed Platforms unify these modalities, allowing simultaneous marker detection and spatial co-localization, thereby accelerating diagnostics and bridging cytopathology with clinical application..(fig.15.A)...

SC(H)HE

mmuno-microfluidic Chips selectively capture CD8+ T lymphocytes via antibody-functionalized microstructures, enabling precise CD8/CD3 antigen analysis with minimal samples for oncology and infectious disease diagnostics. Deformability Cytometry complements this by probing F-actin networks under flow strain to reveal cytoskeletal abnormalities. Nucleus Morphology Mapping tracks apoptosis, mitosis, and therapeutic responses through fluorescence imaging, while Single-Cell Encapsulation ensures high-throughput analysis. Integrated multiplexed platforms unify these modalities, delivering rapid, comprehensive disease profiling and bridging cytopathology with clinical application.(fig.15.B)...

Q(H)HE

Immuno-microfluidic Chips use antibody-coated microstructures to capture CD8+ T lymphocytes, enabling accurate CD8/CD3 antigen analysis from very small samples. Deformability Cytometry examines F-actin networks under flow strain to uncover cytoskeletal defects, while Nucleus Morphology Mapping employs fluorescence imaging to monitor apoptosis, mitosis, and treatment responses. Single-Cell Encapsulation boosts throughput with droplet-based assays, and integrated multiplexed platforms combine all these methods, allowing simultaneous marker detection and co-localization. Together, they provide rapid diagnostics and comprehensive disease profiling, effectively linking cellular pathology with clinical application.(fig.15.C)...

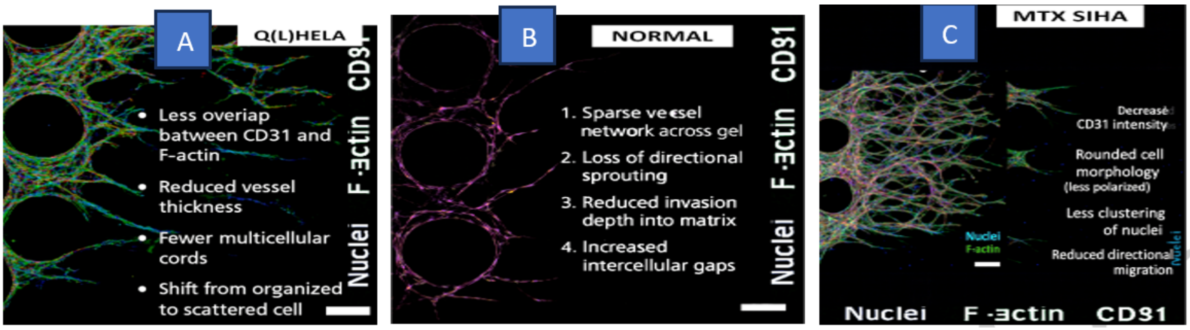

Figure 16:MICROFLUIDIC ASSAY ,A)Q(L)HELA,B)NORMAL(HE),C)MTX SIHA

Immuno-microfluidic Chips provide targeted isolation of CD8+ T lymphocytes through antibody-functionalized microstructures, enabling accurate CD8/CD3 antigen profiling from minimal sample volumes in oncology and infectious disease research. Deformability Cytometry examines F-actin networks under fluid strain to uncover cytoskeletal defects, while Nucleus Morphology Mapping uses fluorescence imaging to monitor apoptosis, mitosis, and therapeutic outcomes. Droplet-based Single-Cell Encapsulation expands throughput, and integrated multiplexed platforms combine these complementary methods, allowing simultaneous marker detection and spatial co-localization. Together, they deliver rapid diagnostics and comprehensive disease profiling, effectively linking cellular pathology with clinical practice..(fig.16.A)...

NORMAL(HE)

High-fidelity immune characterization begins with Immuno-microfluidic Chips, which employ antibody-functionalized microstructures to selectively capture CD8+ T lymphocytes, enabling precise CD8/CD3 antigen profiling from minimal samples. This biochemical interrogation is complemented by Deformability Cytometry, where F-actin networks are subjected to flow strain to reveal cytoskeletal instabilities. Cellular dynamics are then monitored through Nucleus Morphology Mapping, using fluorescence imaging to track apoptosis, mitosis, and therapeutic responses. Droplet-based Single-Cell Encapsulation expands throughput, allowing detailed analysis of individual cellular components. Finally, integrated multiplexed platforms merge these distinct modalities, achieving simultaneous marker detection and spatial co-localization. Together, they deliver rapid diagnostics and comprehensive disease profiling, effectively bridging cytopathology with clinical application..(fig.16.B)...

MTX(SI)

Deformability cytometry assesses F-actin structure under controlled flow stress to reveal mechanical cell abnormalities. Nuclear morphology imaging tracks apoptosis, mitosis, and therapy responses at single-cell resolution, while single-cell encapsulation supports high-throughput analysis. When combined in multiplexed microfluidic platforms, these approaches enable simultaneous biomarker detection and co-localization, providing rapid, precise, and clinically relevant disease profiling..(fig.16.C)...

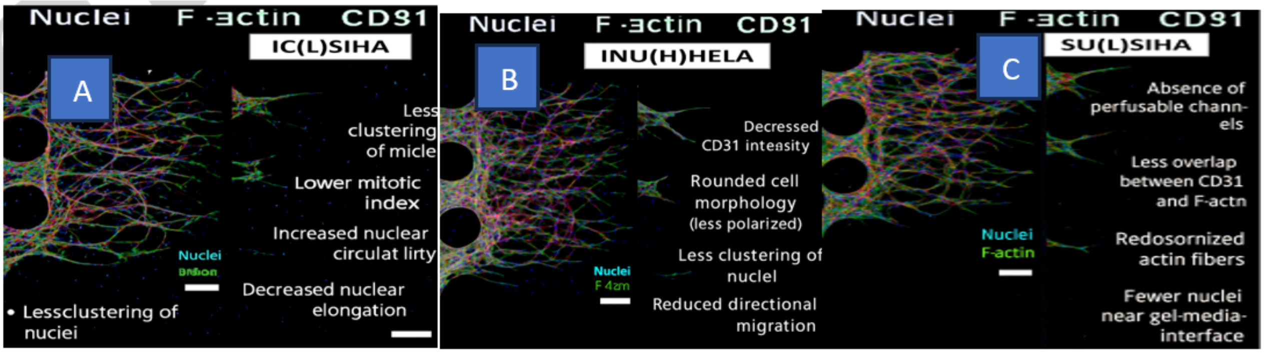

Figure 17:MICROFLUIDIC ASSAY ,A)IC(L)SI,B)INU (H)He,C)SU(L)SI,

IC(L)HE

Deformability cytometry supports this analysis by examining F-actin organization under fluidic stress to identify structural and mechanical cell alterations.Fluorescence-based nuclear morphology assessment monitors apoptosis, cell proliferation, and therapy-related changes at the single-cell level, while single-cell encapsulation technologies permit rapid, high-throughput evaluation. When combined within multiplexed microfluidic platforms, these approaches facilitate concurrent biomarker detection and spatial correlation, providing fast, comprehensive disease characterization and effectively connecting laboratory cytopathology with clinical diagnostics.(fig.17.A)...

INU(H)HE

Advanced immuno-microfluidic systems enable precise immune profiling by isolating $CD8^+$ T cells for accurate CD8/CD3 analysis from minimal samples. Deformability cytometry evaluates F-actin structure under flow stress to detect cellular abnormalities. Fluorescent nuclear imaging tracks apoptosis and mitosis, while single-cell encapsulation supports high-throughput analysis. Integrated multiplexed platforms provide rapid, comprehensive, and clinically relevant disease characterization.(fig.17.B)...

SU(L)SI

High-fidelity immune profiling begins with Immuno-microfluidic Chips, which employ antibody-functionalized microchannels to selectively capture CD8+ T lymphocytes, enabling accurate CD8/CD3 antigen analysis from minimal samples in oncology and infectious disease research. Deformability Cytometry probes F-actin networks under flow strain to reveal cytoskeletal abnormalities, while Nucleus Morphology Mapping uses fluorescence imaging to monitor apoptosis, mitosis, and therapeutic responses. Droplet-based Single-Cell Encapsulation expands throughput, and integrated multiplexed platforms unify these modalities, allowing simultaneous marker detection and spatial co-localization. Together, they deliver rapid diagnostics and comprehensive disease profiling, effectively bridging cytopathology with clinical application.Deformability Cytometry complements this by probing F-actin networks under flow strain to detect cytoskeletal abnormalities. Nucleus Morphology Mapping tracks apoptosis, mitosis, and therapeutic responses via fluorescence imaging, while Single-Cell Encapsulation ensures high-throughput analysis. Integrated multiplexed platforms unify these modalities, enabling simultaneous marker identification and co-localization, delivering rapid, comprehensive disease profiling and bridging cytopathology with clinical application.(fig.17.C)...

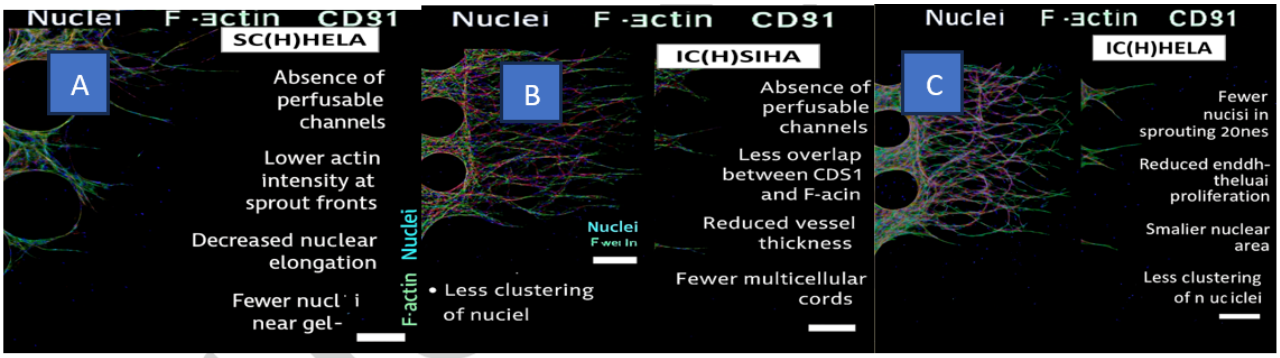

Figure 18:MICROFLUIDIC ASSAY ,A)SC(H)HE,B)IC(H)SI,C)IC(H)He

SC(H)HE

Advanced immunological profiling is driven by Immuno-microfluidic Chips, which capture CD8+ T lymphocytes through antibody-functionalized microchannels, enabling precise CD8/CD3 antigen analysis from minimal samples. Deformability Cytometry reveals F-actin cytoskeletal abnormalities under flow strain, while Nucleus Morphology Mapping tracks apoptosis, mitosis, and therapeutic responses. Single-Cell Encapsulation expands throughput, and integrated multiplexed platforms unify these modalities, delivering rapid, comprehensive disease profiling that bridges cytopathology with clinical practice(fig.18.A)...

IC(H)SI

Comprehensive immunological profiling employs Immuno-microfluidic Chips to capture CD8+ T lymphocytes via antibody-functionalized microchannels, enabling precise CD8/CD3 antigen analysis from minimal samples. Deformability Cytometry reveals F-actin cytoskeletal abnormalities under flow strain, while Nucleus Morphology Mapping tracks apoptosis, mitosis, and therapeutic responses through fluorescence imaging. Single-Cell Encapsulation expands throughput, and integrated multiplexed platforms unify these modalities, delivering rapid diagnostics and bridging cytopathology with clinical practice(fig.18.B).

IC(H)HE

Execution of high-fidelity immune profiling employs Immuno-microfluidic Chips to capture CD8+ T lymphocytes via antibody-functionalized microchannels, enabling precise CD8/CD3 antigen analysis from minimal samples. Deformability Cytometry reveals F-actin cytoskeletal abnormalities under flow strain, while Nucleus Morphology Mapping tracks apoptosis, mitosis, and therapeutic responses. Single-Cell Encapsulation expands throughput, and integrated multiplexed platforms unify these modalities, delivering rapid diagnostics and comprehensive disease profiling that bridges cytopathology with clinical practice.(fig.18.C)...

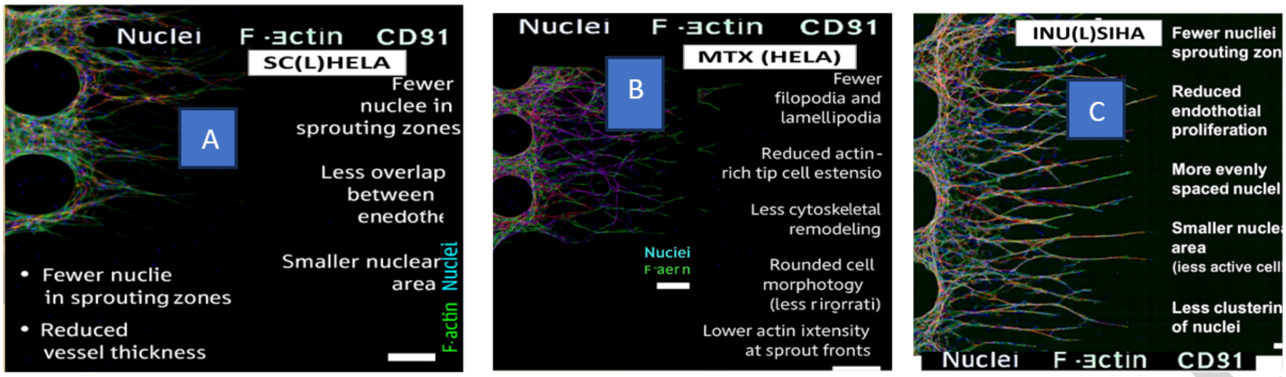

Figure 19:MICROFLUIDIC ASSAY ,A)IC(L)HE,B)MTX(HE),C)INU(L)SI

SC(L)HE

Refined immunological characterization is enabled by Immuno-microfluidic Chips, which capture CD8+ T lymphocytes through antibody-functionalized microchannels, allowing precise CD8/CD3 antigen analysis from minimal samples. Deformability Cytometry identifies F-actin cytoskeletal abnormalities under flow strain, while Nucleus Morphology Mapping tracks apoptosis, mitosis, and therapeutic responses. Single-Cell Encapsulation expands throughput, and integrated multiplexed platforms unify these modalities, delivering rapid diagnostics and comprehensive disease profiling that bridges cytopathology with clinical practice.(fig.19.A)...

MTX(HE)

F-actin networks to flow-induced strain, revealing cytoskeletal abnormalities linked to disease progression. Nucleus Morphology Mapping employs fluorescence microscopy to monitor apoptosis, mitosis, and therapeutic responses, while Single-Cell Encapsulation enables high-throughput analysis of nuclei, CD8/CD3, and F-actin. Integrated multiplexed platforms unify these modalities, allowing simultaneous marker detection and co-localization, delivering rapid diagnostics and comprehensive disease profiling that bridges cytopathology with clinical practice.(fig.19.B)...

INU(L)SI

Nucleus Morphology Mapping employs fluorescence microscopy, often with DAPI, to monitor nuclear topography and track apoptosis, mitosis, and therapeutic responses. Single-Cell Encapsulation broadens diagnostics through droplet-based microfluidics, enabling high-throughput analysis of nuclei, CD8/CD3, and F-actin. Integrated multiplexed platforms consolidate these modalities, allowing simultaneous marker detection and co-localization, delivering rapid diagnostics and comprehensive disease profiling that bridges cytopathology with clinical intervention.(fig.19.C)...

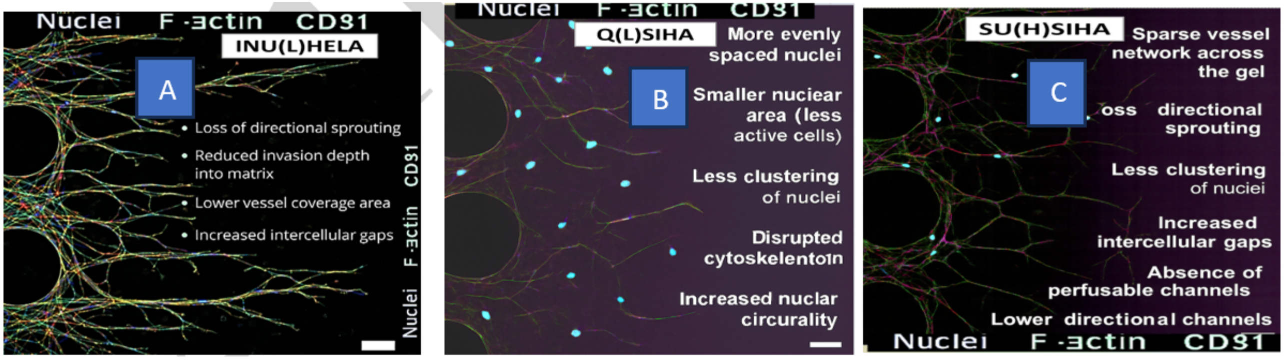

Figure 20:MICROFLUIDIC ASSAY ,A)INU(L)HE,B)Q(L)SI,C)SU(H)SI

INU(L)HE

Nucleus Morphology Mapping employs fluorescence microscopy, often with DAPI, to monitor nuclear topography and track apoptosis, mitosis, and therapeutic responses. Single-Cell Encapsulation broadens diagnostics through droplet-based microfluidics, enabling high-throughput analysis of nuclei, CD8/CD3, and F-actin. Integrated multiplexed platforms unify these modalities, allowing simultaneous marker detection and spatial co-localization. This comprehensive integration accelerates diagnostic turnaround, enhances disease profiling, and bridges fundamental cytopathology with clinical intervention, while morphological and cytoskeletal indicators confirm reduced motility, proliferation, and angiogenesis.(fig.20.A)

Q(L)SI

Nuclear morphology reveals suppressed motility through increased circularity, decreased elongation, smaller nuclear area, and rounded cell shape. Spatial dynamics show reduced proliferation via evenly spaced, less clustered nuclei, lower mitotic index, and limited chemotaxis. Angiogenic inhibition is evidenced by sparse vessels, reduced CD31, and impaired sprouting. Structural disruption and cytoskeletal disarray—marked by weakened adhesion, intercellular gaps, and diminished actin remodeling—confirm impaired migration, invasion, and angiogenesis.(fig.20.B)...

SU(H)SI

Cytoskeletal and Adhesion Dynamics,Increased intercellular gaps: Interpreted as weakened cell-cell adhesion, this suggests cytoskeletal disruption and reduced cohesion.Leading-Edge Dynamics: Reduced actin-rich tip cell extension and fewer filopodia or lamellipodia indicate diminished cytoskeletal activity and weakened dynamics at the sprout fronts, reflecting suppressed migration and sprouting drive.Cytoskeletal Disarray: Reorganized actin fibers and reduced cytoskeletal remodeling reflect a static or disorganized network, indicating impaired motility and structural plasticity(fig.20.C).

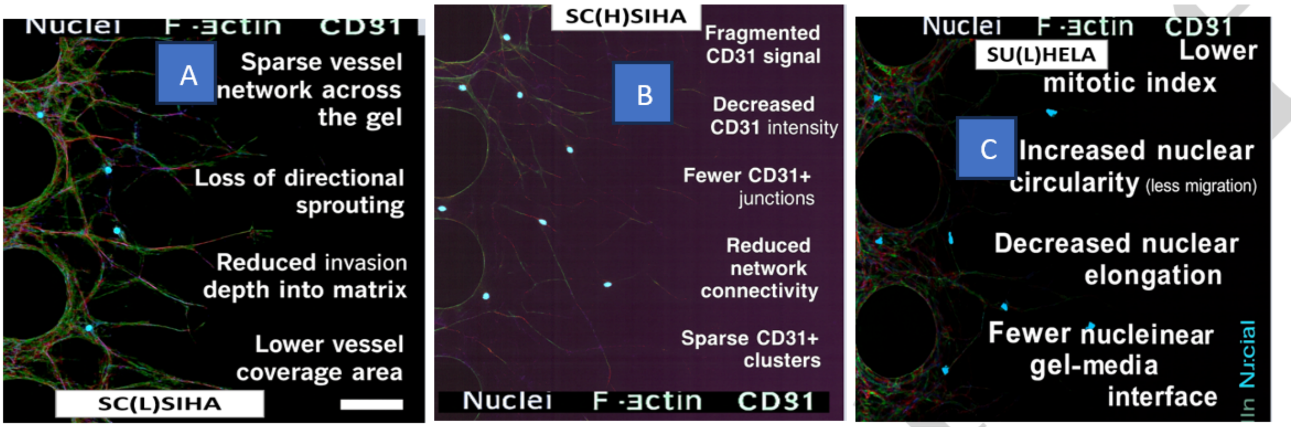

Figure 21:MICROFLUIDIC ASSAY ,A)SC(L)SI,B)SC(H)SI,C)SU(L)HE

SC(L)SI

Therapeutic efficacy is demonstrated by marked morphometric and spatial alterations indicating cellular arrest and structural disruption. Increased nuclear circularity, reduced elongation, and rounded morphology reflect suppressed motility and decreased metabolic activity. Reduced mitotic index and nuclear clustering confirm proliferative inhibition. Impaired angiogenesis, weakened vascular integrity, diminished invasion, and cytoskeletal disorganization collectively signify loss of coordinated migration and structural stability.(fig.21.A).

SC(H)SI

Therapeutic evaluation highlights cellular stasis and disrupted architecture. Nuclear circularity, reduced elongation, smaller area, and rounded morphology signify suppressed motility, diminished stress, and limited chromatin remodeling. Even nuclear spacing, reduced clustering, and lower mitotic index confirm proliferative restraint. Sparse vasculature, diminished CD31, impaired sprouting, widened gaps, and cytoskeletal disarray collectively demonstrate angiogenic inhibition, weakened adhesion, and a profound loss of migratory capacity.(fig.21.B).

SU(L)HE

The comprehensive evaluation of therapeutic impact is achieved through the systematic analysis of morphometric and spatial indicators, which reveal a definitive shift toward cellular stasis and structural disruption. Nuclear circularity, reduced elongation, smaller area, and rounded morphology indicate suppressed motility, diminished stress, and limited chromatin remodeling. Even nuclear spacing, reduced clustering, and lower mitotic index confirm proliferative restraint. Sparse vasculature, reduced CD31, impaired sprouting, widened gaps, and cytoskeletal disarray collectively demonstrate angiogenic inhibition, weakened adhesion, and a profound loss of migratory potential.(fig.21.C).

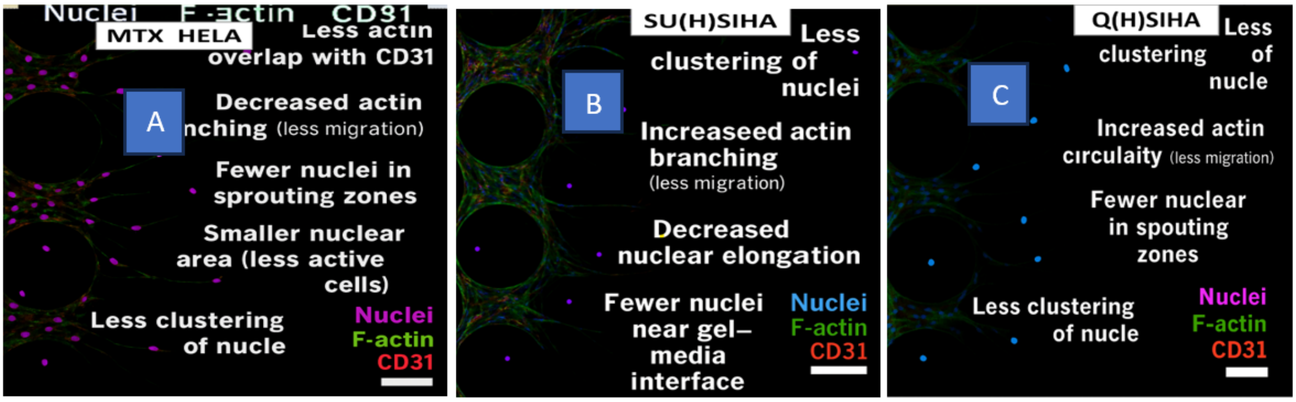

Figure 22:MICROFLUIDIC ASSAY ,A)MTX(HE),B)SU(H)SI,C)Q(H)SI

MTX(HE)

The observed **increased nuclear circularity** and **diminished nuclear elongation** signal a transition to a less polarized state, reflecting suppressed motility, reduced mechanical stress, and limited chromatin remodeling. This is corroborated by a **rounded cell morphology** and **smaller nuclear area**, which indicate a non-migratory phenotype and a significant decline in transcriptional and mitotic engagement. Proliferative suppression is further evidenced by **more evenly spaced nuclei**, **less clustering of nuclei**, and a **lower mitotic index**, which collectively suggest the mitigation of uncontrolled expansion and weakened intercellular adhesion.

Significant vascular and structural disruption is evidenced by a **sparse vessel network** and the **absence of perfusable channels**, confirming impaired angiogenesis and compromised vessel formation. These findings are reinforced by a **loss of directional sprouting**, **reduced invasion depth**, and **fewer multicellular cords**, indicating a failure in collective migration and guided endothelial movement. Finally, **increased intercellular gaps** and **weakened leading-edge dynamics**—characterized by lower actin intensity at sprout fronts and reduced exploratory filopodia—confirm extensive cytoskeletal disarray and a profound loss of migratory and sprouting drive(fig.22.A).

SU(H)SI

Systematic analysis of morphometric and spatial data defines therapeutic efficacy, revealing cellular stasis and disrupted architecture. Nuclear circularity, reduced elongation, smaller area, and rounded morphology indicate suppressed motility, diminished stress, and limited chromatin remodeling. Even nuclear spacing, reduced clustering, and lower mitotic index confirm proliferative restraint. Sparse vasculature, impaired sprouting, widened gaps, and cytoskeletal disarray collectively demonstrate angiogenic inhibition, weakened adhesion, and loss of migratory drive.(fig.22.B).

Q(H)SI

Therapeutic analysis demonstrates cellular stasis and disrupted organization. Nuclear circularity, reduced elongation, smaller area, and rounded morphology signify suppressed motility, diminished stress, and limited chromatin remodeling. Even nuclear spacing, reduced clustering, and lower mitotic index confirm proliferative restraint. Sparse vasculature, impaired sprouting, widened intercellular gaps, and weakened actin dynamics collectively reveal angiogenic inhibition, compromised adhesion, cytoskeletal disarray, and a profound loss of migratory capacity.(fig.22.C).

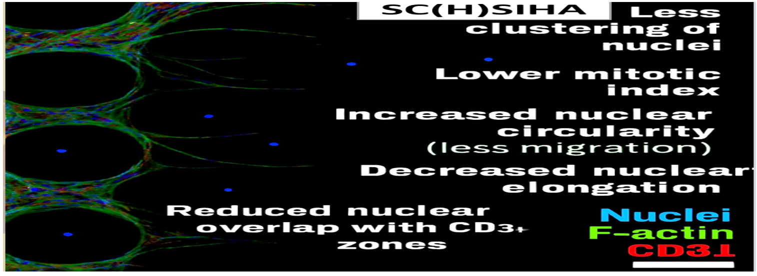

Figure 23:MICROFLUIDIC ASSAY ,SC(H)SI

SC(H)SI

The observed **increased nuclear circularity** signals a transition to a less polarized morphology, suggesting suppressed motility and reduced chromatin remodeling. This is corroborated by a **diminished nuclear elongation**, which reflects lower mechanical stress and transcriptional activity, thereby indicating reduced motility and metabolic engagement. Even nuclear spacing, reduced clustering, and lower mitotic index confirm proliferative restraint. Sparse vasculature, impaired sprouting, widened gaps, and weakened actin dynamics collectively demonstrate angiogenic inhibition, compromised adhesion, cytoskeletal disarray, and loss of migratory drive.(fig.23).

Author for Correspondence: csaha320@rku.ac.in

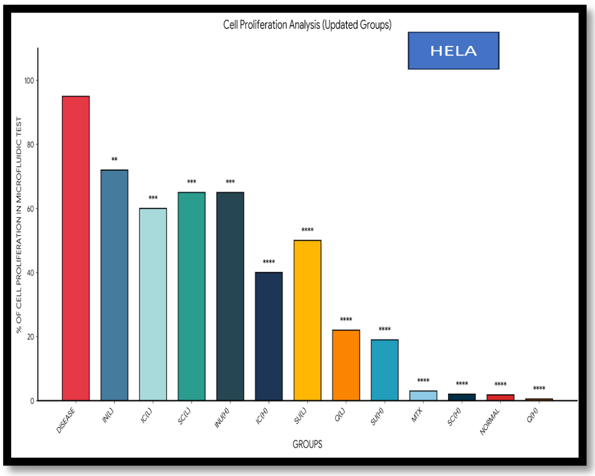

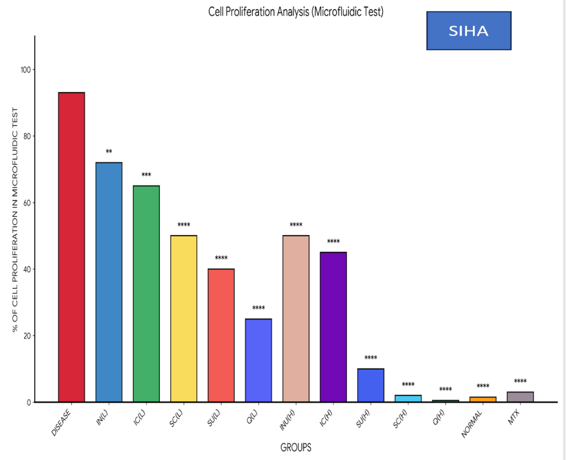

The therapeutic efficacy of the experimental treatments on the HELA cell line was quantified by comparing proliferation percentages against the DISEASE control group, which displayed a baseline density of approximately 95%. Statistical analysis revealed varying degrees of success, beginning with the IN(L) group, which showed an initial reduction to 72% (P < 0.01$, denoted by **). A more robust suppression of cell division and nuclear expansion was observed in the IC(L), SC(L), and INU(H) groups, which reduced proliferation to between 60% and 65% (P < 0.001, denoted by ***). The most significant therapeutic impacts (P < 0.0001, denoted by ****) were achieved by the IC(H), SU(L), Q(L), and SU(H) groups, which demonstrated a marked loss of directional sprouting and weakened cell-cell adhesion. Near-total proliferative arrest was recorded in the MTX and SC(H) groups (~2–3% proliferation), while the Q(H) group exhibited the maximum observed efficacy, suppressing proliferation to less than 1% relative to the disease state.

These high-significance results (P < 0.0001$) are directly corroborated by a suite of morphometric shifts, specifically a lower mitotic index and smaller nuclear areas that reflect reduced metabolic engagement. Spatially, these treatments resulted in more evenly spaced nuclei and less clustering, indicating a transition from uncontrolled crowding to a uniform distribution. Furthermore, the treatment effectively impaired chemotaxis and endothelial migration, evidenced by fewer nuclei near the gel-media interface and in sprouting zones. This comprehensive structural failure is further defined by the absence of perfusable channels and loss of directional sprouting, confirming a total disruption of angiogenic morphogenesis and cytoskeletal stasis.

In the SIHA and HELA cell line proliferation analyses, therapeutic efficacy was quantified by comparing treatment groups against the DISEASE group, which showed the highest proliferative baseline (approximately 94%). The IN(L) group initiated suppression at P < 0.01 (), while the IC(L), SC(L) (for HELA), and INU(H) (for HELA) groups demonstrated more robust anti-proliferative activity at P < 0.001 (). *For both cell lines, the most substantial therapeutic impacts were achieved by the SU(L), Q(L), IC(H), SU(H), SC(H), and Q(H) groups, all reaching maximum statistical significance at P < 0.0001 (***)*. Near-total inhibition of proliferation was recorded in the MTX, SC(H), and Q(H) groups, with Q(H) exhibiting the highest efficacy at less than 1% proliferation.

These significant outcomes are corroborated by specific phenotypic shifts:

Proliferative Arrest: A lower mitotic index and smaller nuclear area reflect reduced metabolic engagement and lower transcriptional/mitotic activity.

Spatial and Structural Stability: More evenly spaced nuclei and less clustering indicate uniform distribution and weakened cell-cell adhesion.

Invasive and Angiogenic Suppression: Impaired chemotaxis is confirmed by fewer nuclei near the gel-media interface and reduced invasion depth.

Vascular Failure: Functional disruption is evidenced by a sparse vessel network, an absence of perfusable channels, and loss of directional sprouting, confirming compromised vascular development and impaired angiogenic guidance.

Cytoskeletal Disarray: Increased intercellular gaps and a disrupted cytoskeleton signify a loss of structural integrity and polarity, further indicating suppressed motility and chromatin remodeling.

3.5.Result & Discussions of Tube Formation assay for in-vivo method:

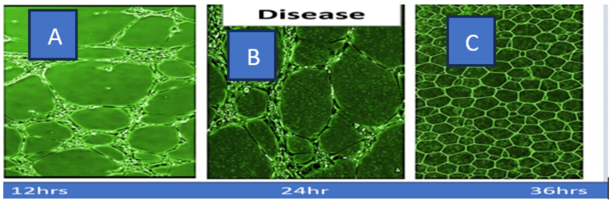

Figure 24:TUBE FORMATION ASSAY ,DISEASEA)12HRS,B)24HRS,C)36HRS

DISEASE(HE)

The temporal progression of vascular development within the disease group was characterized by distinct morphological stages observed over a 36-hour period. At the 12-hour interval, the initiation of vascular sprouting was noted, marked by the emergence of capillary-like strands and early nodal points(fig.24.A). These features indicated the onset of angiogenic signaling and VEGF-driven endothelial activation, which served as the foundation for structured network formation. By 24 hours, the culture transitioned into an intermediate vascular mesh featuring stable junctions and interconnected strands. This stage showed increased branching and moderate vessel density, representing functional angiogenesis capable of supporting tissue perfusion and metabolic demands(fig.24.B).

At the 36-hour mark, the architecture evolved into a dense and coherent vascular network. This terminal stage was defined by high node density, symmetrical branching, and strong intercellular cohesion, signifying successful remodeling and integration into the tissue microenvironment. Overall, the disease group exhibited structured and functional angiogenesis characterized by progressive vessel formation and spatial coherence. These observations represent the hallmarks of regulated angiogenesis, which is essential for supporting tissue viability, physiological remodeling, and repair(fig.24.C).

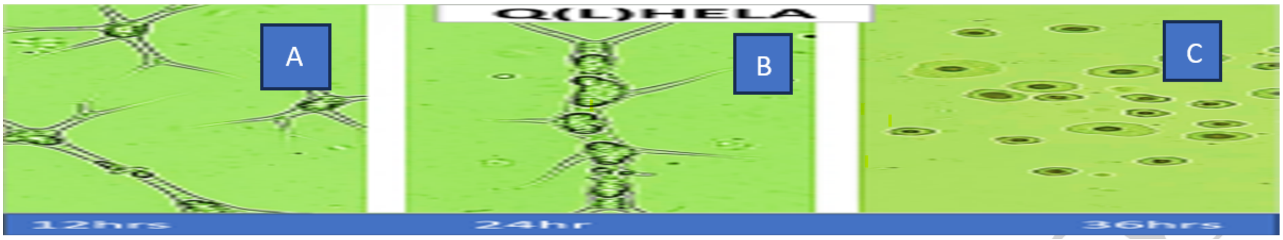

Figure 25:TUBE FORMATION ASSAY Q(L)HE ,A)12HRS,B)24HRS,C)36HRSQ(L)HE

Q(L)HELA

In contrast, the treatment group demonstrated an inhibited morphology and a significant loss of network coherence. Observations at 12 hours revealed elongated cells with sparse branching and long processes, yet minimal interconnectivity and weak nodal formation were present(fig.25.A). . This indicated that the treatment successfully inhibited initial branching and directional alignment. By 24 hours, the cells appeared as compact bodies with reduced projections, shortened processes, and irregular contours(fig.25.B). . These morphological changes suggested that drug-induced stress impaired cytoskeletal dynamics, thereby disrupting stabilization and spatial expansion. While a complex network was noted at 36 hours, it was characterized by poor geometric symmetry and multiple disorganized branching processes. This lack of architectural maturation confirmed that the treatment effectively blocked the development of functional architecture. Collectively, the treatment elicited a robust inhibitory response, disrupting pathological expansion and the formation of organized signaling domains.

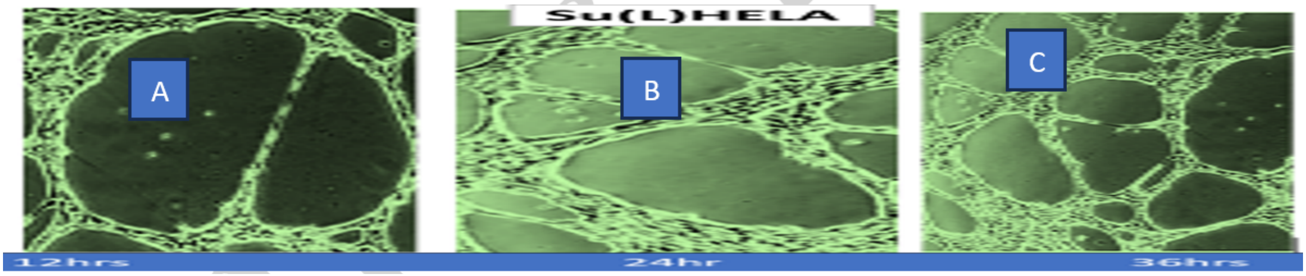

Figure 26:TUBE FORMATION ASSAY SU(L)HE ,A)12HRS,B)24HRS,C)36HRS

SU(L)HE

The anti-cancer drug suppressed malignant progression across time points. At 12 hours, cancer cells showed elongated but poorly branched processes, indicating inhibited outgrowth(fig.26.A). . By 24 hours, compact bodies with shortened projections and irregular contours reflected cytoskeletal stress(fig.26.B). . At 36 hours, networks appeared asymmetrical despite connectivity(fig.26.C).. Overall, therapy blocked maturation, impaired organization, and inhibited angiogenesis, adhesion, and invasive drive.

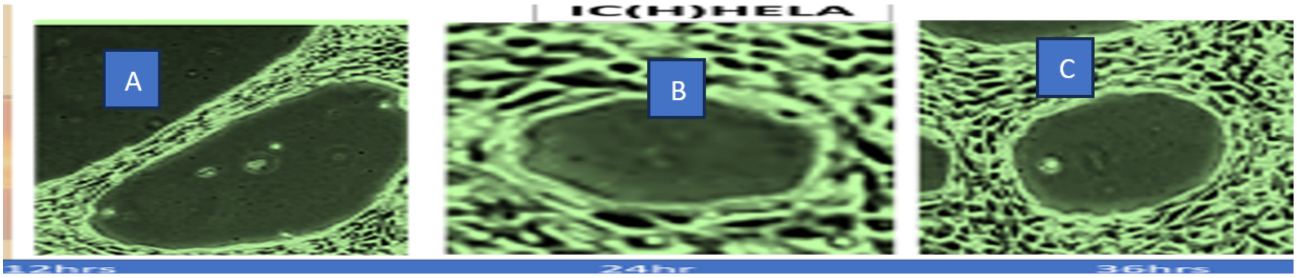

Figure 27:TUBE FORMATION ASSAY IC(H)HE ,A)12HRS,B)24HRS,C)36HRS

IC(H)HE

At 12 hrs, early drug effects are evident with mild reduction in cell spreading and partial disruption of peripheral cellular networks. Cells appear less elongated, indicating the onset of inhibited migration(fig.27.A). At 24 hrs, structural disorganization becomes more prominent. Reduced cell density, weakened intercellular connections, and visible shrinkage of the central mass suggest suppressed proliferation and early cytotoxic effects(fig.27.B).By 36 hrs, marked structural collapse is observed with significant loss of network integrity, decreased cellular clustering, and pronounced rounding of cells. These findings indicate strong anti-proliferative activity, impaired migration, and effective anti-cancer drug action over time(fig.27.C). .

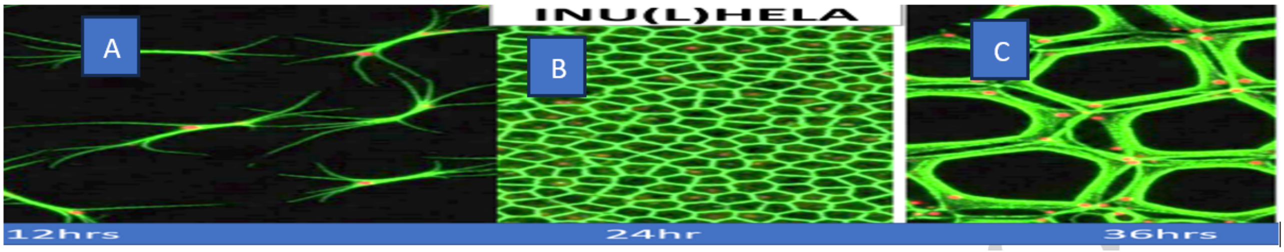

Figure 28: TUBE FORMATION ASSAY INU(L)HE ,A)12HRS,B)24HRS,C)36HRS

INU(L)HE

At **12 hrs**, cells show elongated morphology with thin, branching extensions and initial network formation. The structure appears loosely organized, indicating active migration and early cytoskeletal alignment(fig.28.A).At **24 hrs**, a well-defined, dense honeycomb-like network is observed. Cells display strong intercellular connectivity and uniform structural organization, suggesting peak proliferation and stable cytoskeletal integrity(fig.28.B).By **36 hrs**, the network becomes thicker and more enlarged with widened mesh-like structures(fig.28.C). Although connectivity remains, the architecture appears slightly expanded, indicating advanced structural remodeling and continued cellular interaction over time.

.

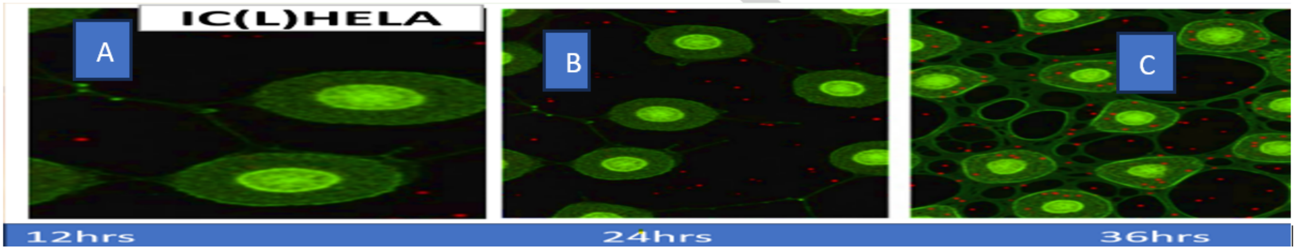

Figure 29:TUBE FORMATION ASSAY IC(L)HE ,A)12HRS,B)24HRS,C)36HRS

IC(L)HE

At 12 hrs, cells appear well-spread with elongated morphology and clear nuclear definition. Intercellular spacing is moderate, indicating active attachment and early proliferative activity(fig.29.a).At 24 hrs, an increase in cell number is observed with reduced intercellular gaps(fig.29.b). Cells show enhanced spreading and closer alignment, suggesting progressive proliferation and strengthened cellular interactions.By 36 hrs, marked cell confluency is evident with dense clustering and minimal spacing between cells. The morphology reflects sustained proliferation, intact cytoskeletal organization, and stable structural integrity over time(fig.29.C).

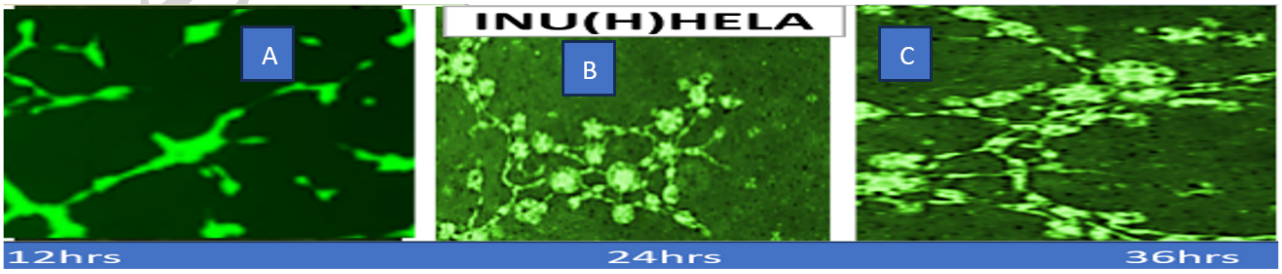

Figure 30:TUBE FORMATION ASSAY INU(L)HE ,A)12HRS,B)24HRS,C)36HRS

**Author for Correspondence: csaha320@rku.ac.in*

INU(L)HE

At 12 hrs, limited and scattered cellular structures are observed with short, incomplete extensions, indicating minimal network formation and reduced initial connectivity(fig.30.A).At 24 hrs, clustered cellular aggregates with radial sprouting become visible(fig.30.B). Although some network development occurs, the structures appear irregular and less organized compared to control conditions.By 36 hrs, partial elongation and interconnected branching structures are present; however, the network remains discontinuous and sparse(fig.30.C). These findings suggest impaired structural organization, reduced coordinated migration, and suppressed angiogenic-like behavior over time

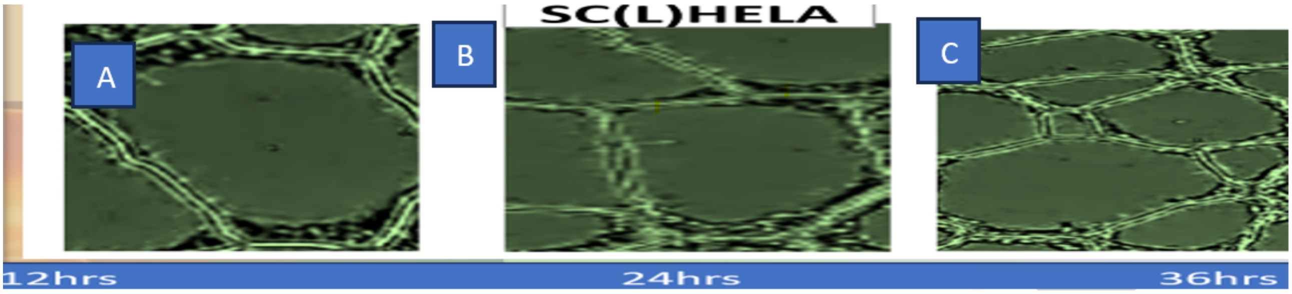

Figure 31:TUBE FORMATION ASSAY SC(L)HE ,A)12HRS,B)24HRS,C)36HRS

SC(L)HE

At 12 hrs, cells display well-defined, polygonal morphology with clear boundaries and moderate intercellular spacing, indicating stable attachment and early structural organization(fig.31.A). .At 24 hrs, increased cell spreading and tighter junction formation are observed(fig.31.B). . The cellular architecture appears more compact, reflecting progressive proliferation and enhanced cell–cell adhesion.By 36 hrs, marked confluency is evident with closely packed polygonal cells and minimal intercellular gaps(fig.31.C). . The uniform morphology and intact structural arrangement suggest sustained growth, strong intercellular connectivity, and maintained cytoskeletal integrity over time

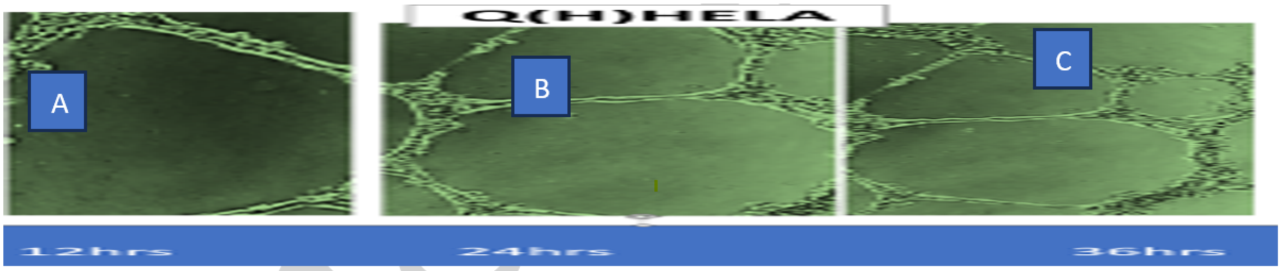

Figure 32:TUBE FORMATION ASSAY Q(H)HE ,A)12HRS,B)24HRS,C)36HRS

Q(H)HE

At 12 hrs, cells exhibit broad spreading with defined peripheral boundaries and early intercellular contacts, indicating stable attachment and initial structural organization(fig.32.A). .At 24 hrs, enhanced cell–cell connectivity and reduced intercellular gaps are observed(fig.32.B). . The architecture appears more continuous, suggesting active proliferation and strengthened structural cohesion.By 36 hrs, dense confluency with closely aligned polygonal cells is evident(fig.32.C). . The uniform morphology and intact cellular framework reflect sustained growth, maintained cytoskeletal stability, and organized structural maturation over time.

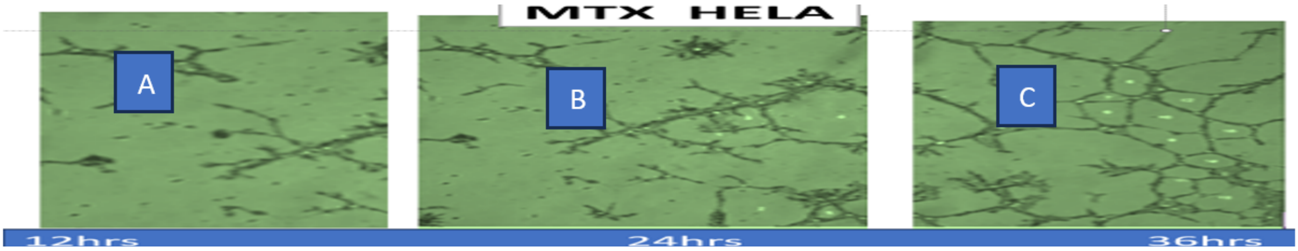

Figure 33:TUBE FORMATION ASSAY MTX(HE) ,A)12HRS,B)24HRS,C)36HRS

MTX(HE)

At 12 hrs, sparse and thin branching structures are visible with discontinuous cellular connections, indicating early inhibition of network formation and reduced cellular spreading(fig.33.A). At 24 hrs, partial elongation and fragmented branching patterns are observed. The network remains irregular and loosely organized, suggesting suppressed proliferation

---

**Author for Correspondence: csaha320@rku.ac.in*

and impaired structural integrity(fig.33.B). .By 36 hrs, although some extended connections appear, the architecture remains fragile and discontinuous with limited density(fig.33.C). . These findings indicate sustained anti-proliferative activity, reduced coordinated migration, and compromised structural stability under MTX treatment.

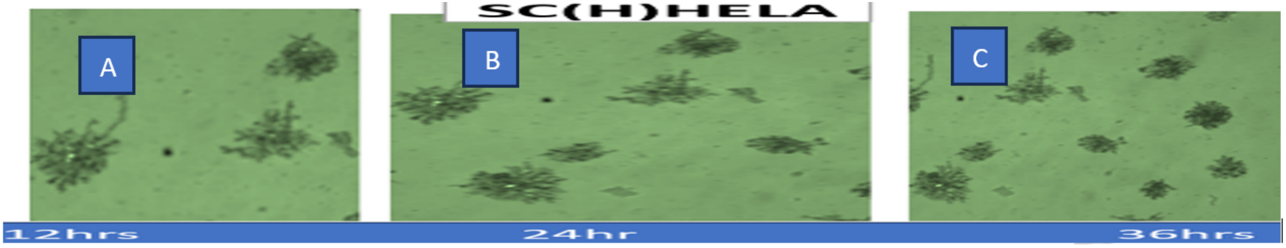

Figure 34:TUBE FORMATION ASSAY SC(H)HE ,A)12HRS,B)24HRS,C)36HRS

SC(H)HE

At 12 hrs, small and scattered cellular clusters are observed with limited spreading and minimal interconnection, indicating early aggregation with restricted migration(fig.34.A). .At 24 hrs, the number and size of compact clusters increase(fig.34.B). . Cells appear tightly packed within aggregates, suggesting enhanced cell–cell adhesion but reduced outward extension.By 36 hrs, multiple dense spheroid-like clusters are evident with clear separation between groups(fig.34.C). . The absence of extensive branching or network formation indicates suppressed migration and a predominantly aggregated growth pattern over time.

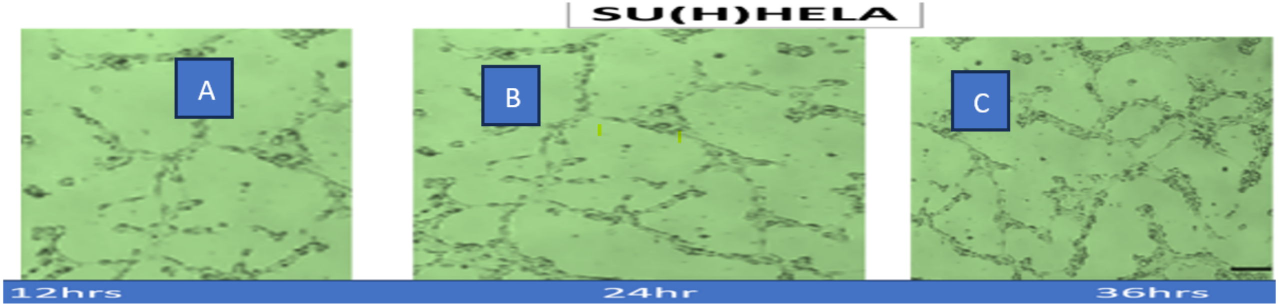

Figure 35:TUBE FORMATION ASSAY SU(H)HE ,A)12HRS,B)24HRS,C)36HRS

SU(H)HE

At 12 hrs, thin and discontinuous cellular strands are visible with scattered cell distribution, indicating weak initial network formation and reduced intercellular cohesion(fig.35.A). .At 24 hrs, partial branching structures emerge; however, the connections remain fragmented and loosely arranged, suggesting limited proliferation and impaired structural organization(fig.35.B). .By 36 hrs, although a broader mesh-like pattern is observed, the network appears irregular with sparse density and incomplete junctions(fig.35.C). . These findings indicate compromised cellular coordination, reduced migration, and diminished structural stability over time.

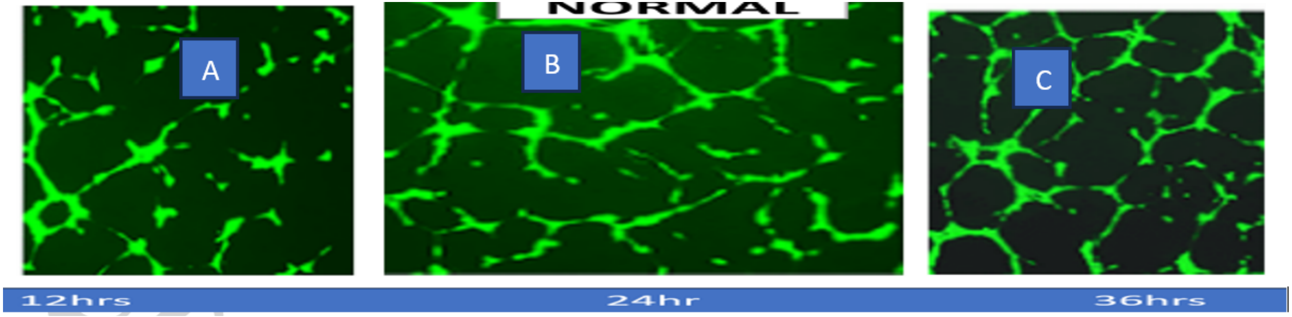

Figure 36:TUBE FORMATION ASSAY NORMAL(HE) ,A)12HRS,B)24HRS,C)36HRS

NORMAL(HE)

At **12 hrs**, initial cellular connections are visible with thin, branching extensions forming early network structures, indicating active migration and cytoskeletal organization(fig.36.A). .At **24 hrs**, a well-defined and dense mesh-like network is observed with strong intercellular connectivity, reflecting robust proliferation and coordinated structural alignment(fig.36.B). .By **36 hrs**, the network becomes more consolidated and uniformly organized with thicker junctions and minimal gaps(fig.36.C). . The intact architecture and continuous branching pattern indicate healthy growth, stable cytoskeletal integrity, and sustained cellular coordination over time.

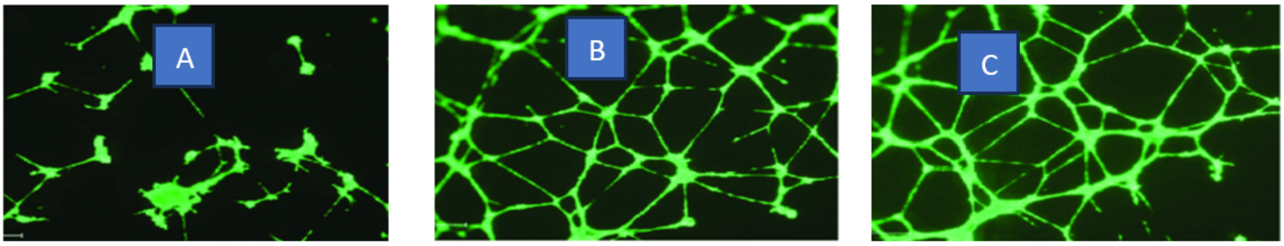

Figure 37:TUBE FORMATION ASSAY NORMAL(SI) ,A)12HRS,B)24HRS,C)36HRS

NORMAL(SI)

At 12 hours, cellular clusters extend elongated processes, signaling early migration and initial gap-bridging(fig.37.A). . By 24 hours, a high-density polygonal lattice emerges as extensions fuse into a continuous, interconnected mesh(fig.37.B). . At 36 hours, the architecture matures into thickened cellular cords with a uniform distribution(fig.37.C). . This stable, consolidated network demonstrates robust structural integrity and the successful completion of a self-sustaining biological pattern across the observed timeframe.

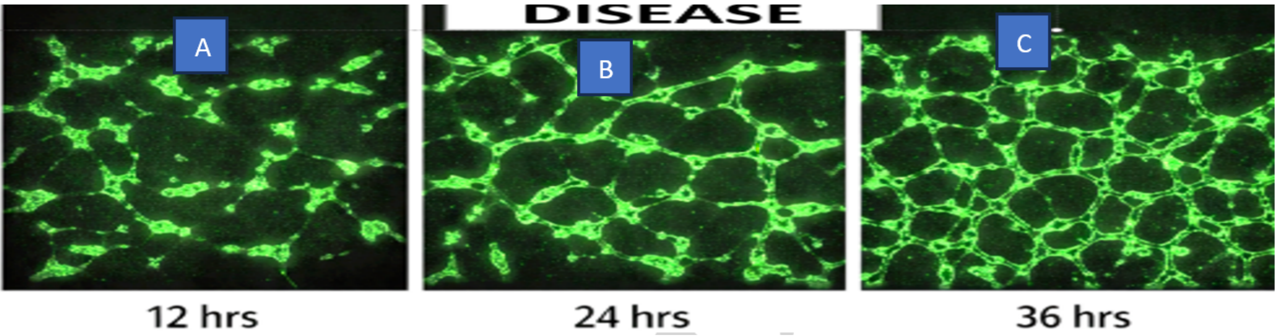

Figure 38:TUBE FORMATION ASSAY DISEAE(SI) ,A)12HRS,B)24HRS,C)36HRS

DISEASE(SI)

At 12 hours, cellular clusters appear fragmented, initiating thin extensions to bridge spatial gaps(fig.38.A). . By 24 hours, these processes fuse into a continuous, albeit irregular, polygonal lattice with emerging nodes(fig.38.B). . By 36 hours, the architecture consolidates into a more uniform, stabilized network with thickened junctions(fig.38.C). . This progression reflects successful cellular migration and structural alignment, establishing a coordinated biological pattern characterized by improved connectivity and reduced architectural gaps over time.

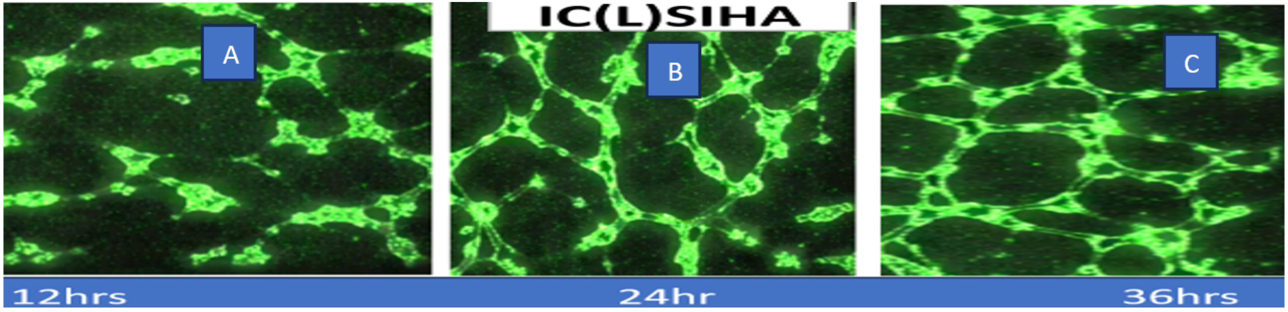

Figure 39:TUBE FORMATION ASSAY IC(L)SI ,A)12HRS,B)24HRS,C)36HRS

IC(L)SI

At 12 hours, cellular clusters extend thin filopodial processes, initiating migratory contact to bridge existing gaps(fig.39.A). . By 24 hours, these extensions fuse into a continuous polygonal lattice, reflecting robust proliferation and coordinated structural alignment(fig.39.B). . By 36 hours, the network reaches a mature, consolidated state with thickened junctions and minimal architectural gaps(fig.39.C). . This stable branching pattern confirms restored cytoskeletal integrity and sustained cellular coordination under treatment.

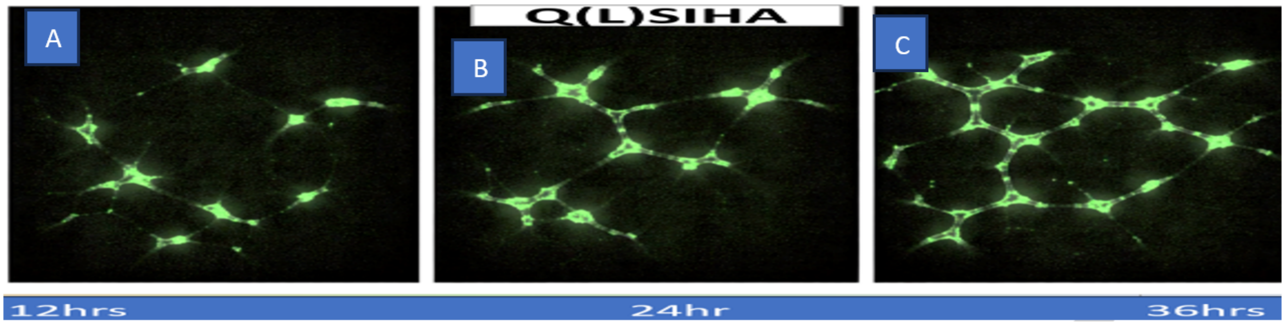

Figure 40:TUBE FORMATION ASSAY Q(L)SI ,A)12HRS,B)24HRS,C)36HRS

Q(L)SI

At 12 hours, cellular clusters extend thin filopodial processes, initiating migratory contact to bridge existing gaps(fig.40.A). . By 24 hours, these extensions fuse into a continuous polygonal lattice, reflecting robust proliferation and coordinated structural alignment(fig.40.B). . By 36 hours, the network reaches a mature, consolidated state with thickened junctions and minimal architectural gaps(fig.40.C). . This stable branching pattern confirms restored cytoskeletal integrity and sustained cellular coordination under treatment.

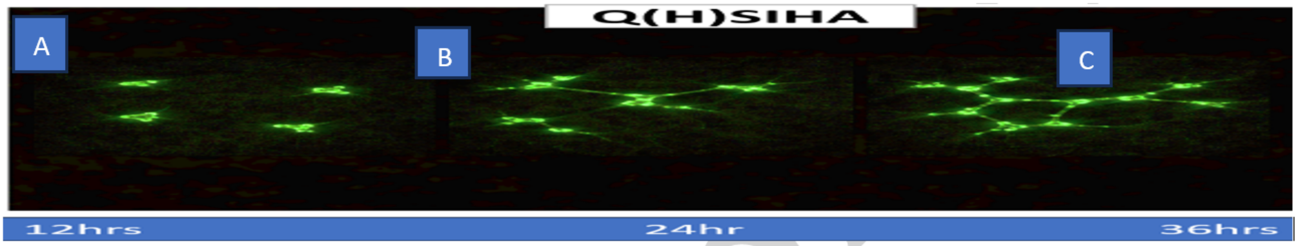

Figure 41:TUBE FORMATION ASSAY Q(H)SI ,A)12HRS,B)24HRS,C)36HRS

Q(H)SI

At 12 hours, cellular clusters extend thin filopodial processes, initiating migratory contact to bridge existing gaps(fig.41.A). . By 24 hours, these extensions fuse into a continuous polygonal lattice, reflecting robust proliferation and coordinated structural alignment(fig.41.B). . By 36 hours, the network reaches a mature, consolidated state with thickened junctions and minimal architectural gaps(fig.41.C). . This stable branching pattern confirms restored cytoskeletal integrity and sustained cellular coordination under treatment.and branching points, indicating the effective suppression of cervical cancer-associated angiogenesis(fig.41.C).

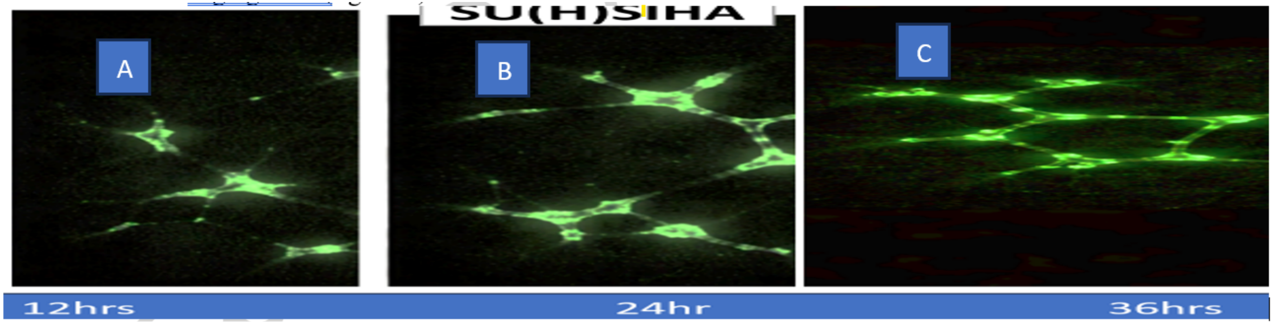

Figure 42:TUBE FORMATION ASSAY SU(H)SI ,A)12HRS,B)24HRS,C)36HRS

SU(H)SI

At 12 hours, cellular clusters remain relatively isolated, extending thin, sporadic filopodia to initiate exploratory migration(fig.42.A). . By 24 hours, these processes fuse into a primitive polygonal lattice characterized by sparse, elongated primary cords and few branching nodes(fig.42.B). . By 36 hours, the architecture matures into a stable, uniform mesh with thickened junctions(fig.42.C). . This regulated progression reflects successful structural coordination and sustained integrity with lower overall network density

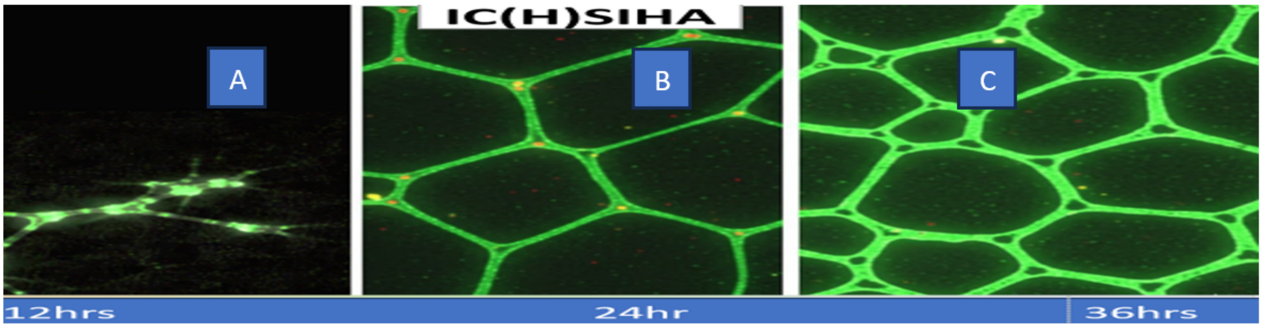

Figure 43:TUBE FORMATION ASSAY IC(H)SI ,A)12HRS,B)24HRS,C)36HRS

IC(H)SI

At 12 hours, IC(H)SIHA exhibits initial cellular clusters that rapidly extend thick processes to bridge extensive gaps(fig.43.A). . By 24 hours, the morphology transitions into a remarkably uniform and well-defined polygonal lattice with high geometric symmetry(fig.43.B). . By 36 hours, the network reaches a mature, stabilized state characterized by robust junctions and thick cellular cords(fig.43.C). . This highly organized architecture reflects superior cytoskeletal integrity and exceptionally coordinated network stabilization over the observed duration.

.

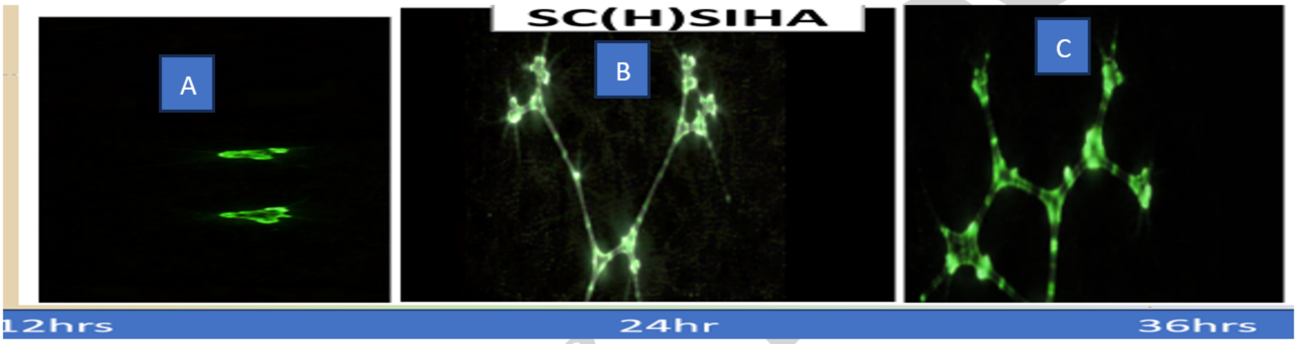

Figure 44:TUBE FORMATION ASSAY SC(H)SI ,A)12HRS,B)24HRS,C)36HRS

SC(H)SI

At 12 hours, cellular clusters remain highly fragmented and isolated, showing minimal exploratory extensions compared to other groups(fig.44.A). . By 24 hours, sparse, elongated primary cords emerge, forming a very loose and incomplete lattice with few branching intersections(fig.44.B). . By 36 hours, the network matures into a simple, stabilized skeletal structure(fig.44.C). . This group maintains significantly lower connectivity and node density than the disease group, reflecting a more inhibited or controlled organizational pace

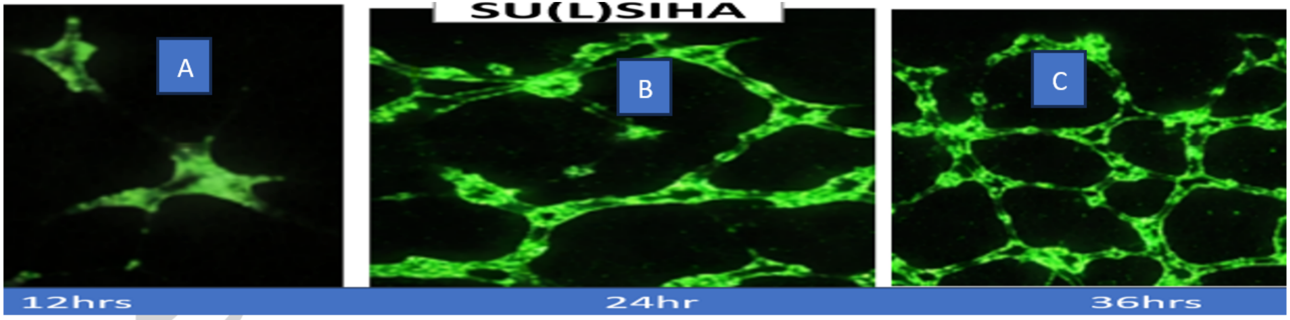

Figure 45:TUBE FORMATION ASSAY SU(L)SI ,A)12HRS,B)24HRS,C)36HRS

SU(L)SI

At 12 hours, cellular presence is extremely minimal, appearing as small, faint dots with almost no visible branching or filopodial extension into the matrix(fig.45.A). . By 24 hours, instead of a mesh, only a few isolated V-shaped or linear cords form, lacking the complex interconnected nodes seen in the disease group(fig.45.B). . By 36 hours, the structure remains a sparse, skeletal framework with wide empty spaces and very few junctions(fig.45.C). . This suggests the SC(H)SIHA treatment significantly restricts network expansion, maintaining a low-density architecture throughout the timeframe.

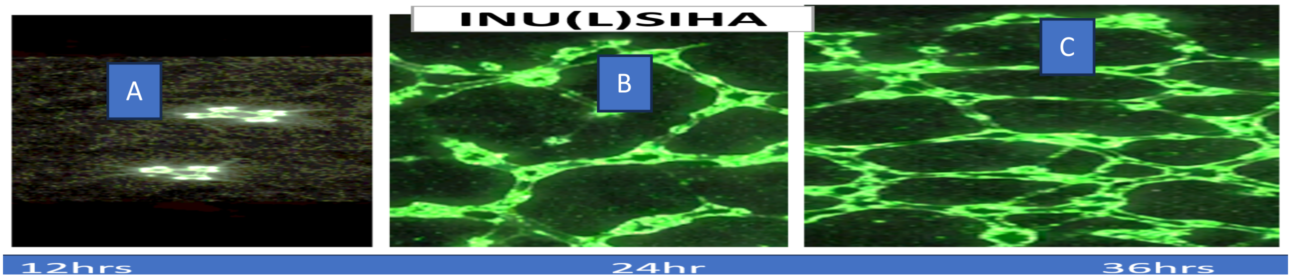

Figure 46:TUBE FORMATION ASSAY INU(L)SI ,A)12HRS,B)24HRS,C)36HRS

INU(L)SI

At **12 hours**, cellular activity is severely restricted, showing only two isolated, faint clusters with virtually no filopodial extensions or migratory progress into the matrix(fig.46.A). . By **24 hours**, the morphology remains underdeveloped, forming a sparse "V-shaped" skeletal framework with only two primary junctions and no complex branching(fig.46.B). . By **36 hours**, the network is still minimal and incomplete, consisting of a few thickened cords that fail to form a closed mesh. This progression indicates that SC(H)SIHA strongly inhibits network formation, maintaining significantly lower connectivity and more architectural gaps than any other group(fig.46.C). .

V

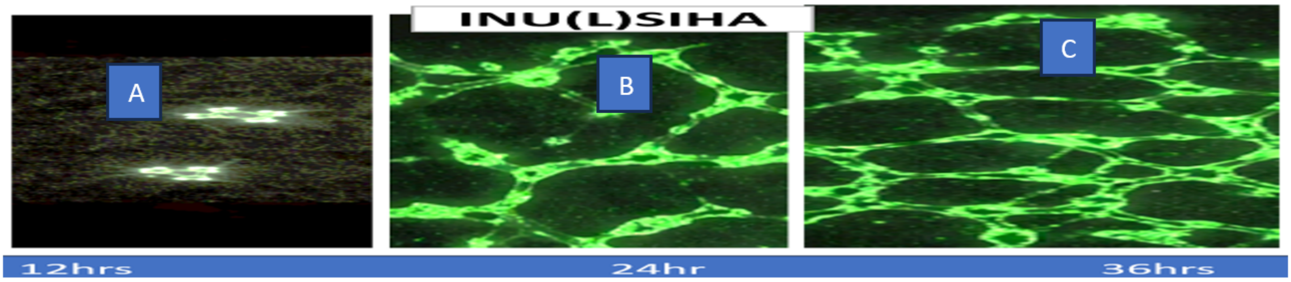

Figure 47:TUBE FORMATION ASSAY INU(L)SI ,A)12HRS,B)24HRS,C)36HRS

INU(H)SI

At **12 hours**, the image shows scattered, elongated cellular islands with minimal filopodial reaching, indicating a delayed start to migratory behavior(fig.47.A). . By **24 hours**, instead of a mesh, the cells form **disjointed, horizontal spindle-like structures** that fail to interconnect vertically, leaving massive longitudinal gaps across the matrix(fig.47.B). . By **36 hours**, the architecture remains highly fragmented and **non-confluent**, consisting of thickened but isolated cellular clusters(fig.47.C). . This development confirms that the INU(H)SIHA treatment effectively disrupts network assembly, preventing the formation of a continuous polygonal lattice compared to the dense disease group

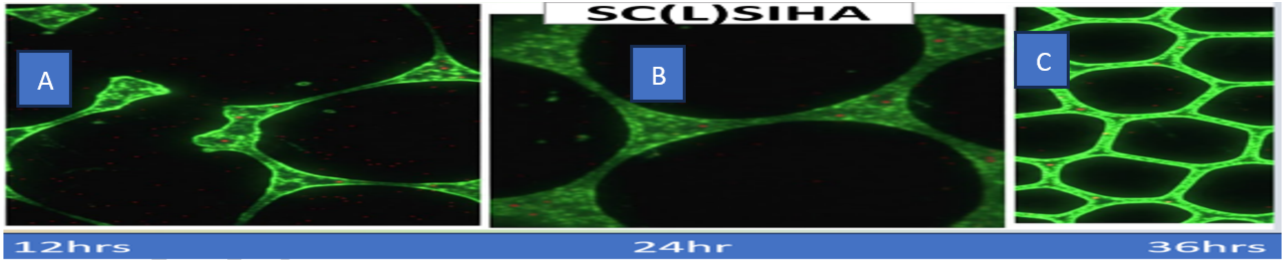

Figure 48:TUBE FORMATION ASSAY SC(L)SI ,A)12HRS,B)24HRS,C)36HRS

SC(L)SI

At **12 hours**, the culture shows widespread, irregular clusters already attempting to bridge gaps(fig.48.A). . By **24 hours**, it forms a very dense, cluttered polygonal lattice(fig.48.B). . At **36 hours**, the network is highly confluent but lacks geometric precision, appearing as a thick, overcrowded mesh with very small, irregular gaps(fig.48.C). .The anti-cancer treatment demonstrated a robust anti-angiogenic response, leading to a comprehensive loss of coordinated cellular architecture across multiple developmental stages.

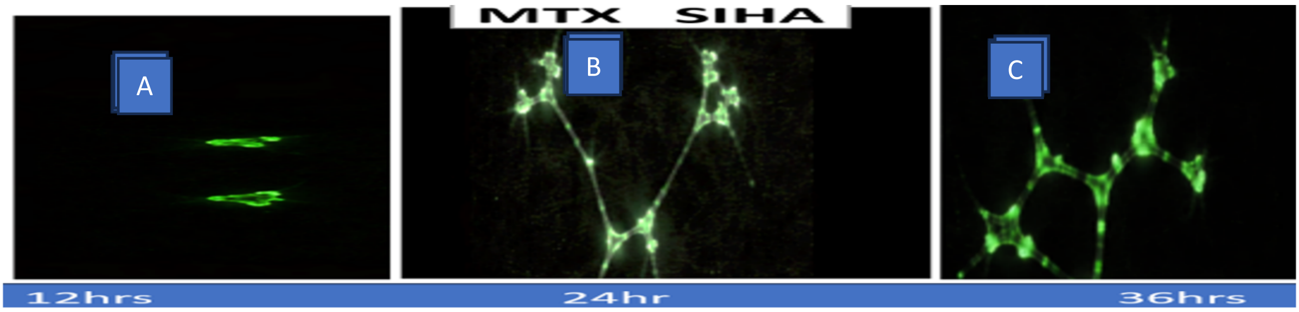

Figure 49:TUBE FORMATION ASSAY MTX(SI) ,A)12HRS,B)24HRS,C)36HRS

MTX(SI)

The standard drug exhibited a potent anti-angiogenic effect, At **12 hours**, the culture displays significant early organization compared to other groups, with robust cellular clusters extending thick, directed processes to initiate contact across the matrix(fig.49.A). . By **24 hours**, these connections rapidly evolve into a remarkably uniform and **geometrically precise polygonal lattice**, showing high symmetry and well-defined cord thickness(fig.49.B). . By **36 hours**, the network reaches a mature, stabilized state characterized by **large, clear geometric openings** and very smooth, thick junctions(fig.49.C). .

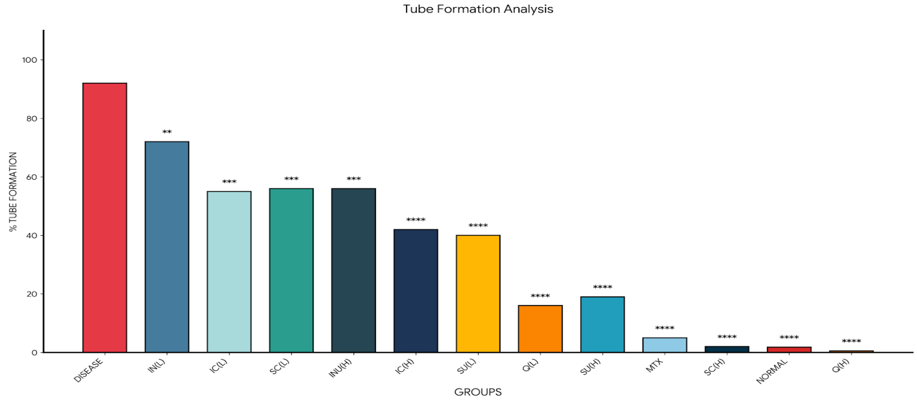

Based on the provided Tube Formation Analysis for HELA cell lines, the DISEASE group (red bar) consistently shows the highest pathological activity, with tube formation levels exceeding 90%. All other experimental groups demonstrate a statistically significant reduction in neovascularization when compared to this disease baseline, categorized as follows:

Statistical Comparison of Treatment Groups

Extreme Significance (p < 0.0001 ****): The majority of treatment groups, including SC(H), Q(H), MTX, SU(H), and Q(L), show the most potent inhibitory response. These groups effectively collapse tube formation to near-zero levels (below 20% in HELA and below 10% in Siha), mirroring the NORMAL control. This statistical result reflects a total failure of the vascular system to form mature meshes, resulting in fragmented, low-density networks.

High Significance (p < 0.001 ***): Intermediate groups such as IC(L), SC(L), and INU(H) show a highly significant reduction compared to the disease state, with tube formation generally ranging between 50% and 60%. Morphologically, these p-values correspond to drug-induced stress that delays structural maturation and fiber compaction, preventing the formation of a cohesive tissue mesh.

Moderate Significance (p < 0.01 **): The IN(L) group shows the least amount of inhibition among the treatments, with tube formation remaining at approximately 72% in both cell lines. While still statistically distinct from the disease group, it indicates a weaker anti-angiogenic response than the higher-dose counterparts.

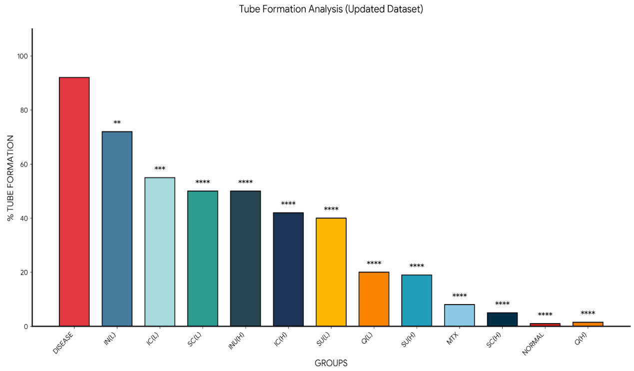

In both the Siha cell line analyses, the DISEASE group (represented by the red bar) demonstrates the highest pathological activity, with tube formation levels exceeding 90%. All treatment groups show a statistically significant reduction in neovascularization compared to this disease baseline, categorized by their respective p-values:

Statistical Comparison of Treatment Groups

Extreme Significance ($p < 0.0001$ ****): The most potent inhibitory response is observed in the majority of treatment groups, including SC(H), Q(H), MTX, SU(H), and Q(L). These treatments effectively collapse tube formation to near-zero levels (below 20% in HELA and below 10% in Siha), matching the NORMAL control group. This statistical data corresponds to a complete failure of the vascular system to mature, resulting in fragmented, low-density networks.

High Significance ($p < 0.001$ ***): Intermediate treatment groups such as IC(L), SC(L) (in HELA), and INU(H) show a highly significant reduction compared to the DISEASE group, with tube formation typically ranging between 50% and 60%. Morphologically, these p-values represent drug-induced stress that actively delays structural maturation and membrane stabilization.

Moderate Significance ($p < 0.01$ **): The IN(L) group exhibits the least amount of inhibition among the treated sets, maintaining tube formation at approximately 72% in both cell lines. While still significantly different from the DISEASE group, it indicates a weaker anti-angiogenic response than high-dose treatments.

4.CONCLUSION

This study implemented a comprehensive multi-assay strategy to evaluate the cytotoxic and functional effects of experimental treatments in cervical cancer models. In the in-vitro setting, the Integrated Cell Demise Assay and MTT assay provided complementary insights into cellular viability, apoptotic and necrotic responses, and metabolic activity, thereby enabling accurate profiling of treatment-induced cell death. Under in-vivo-mimicking conditions, the microfluidic assay facilitated precise evaluation of cellular dynamics within controlled microenvironmental gradients, closely reflecting physiological relevance. Furthermore, the tube formation assay offered functional evidence of treatment impact on angiogenic potential, a critical hallmark of tumor progression.Collectively, these integrated approaches established a robust framework for assessing therapeutic efficacy at morphological, metabolic, and functional levels. The findings demonstrate that the tested compounds exert significant cytotoxic effects, disrupt cellular behavior under microfluidic conditions, and impair angiogenic responses. This multidimensional evaluation strengthens mechanistic interpretation and enhances translational relevance, bridging the gap between conventional in-vitro assays and the complex biological realities of tumor progression. Ultimately, the integration of cell demise analysis, metabolic viability assessment, microfluidic dynamics, and angiogenesis evaluation provides a reliable platform for preclinical screening of anticancer agents and supports the advancement of more effective therapeutic strategies against cervical cancer.

5.ABBREVIATIONS:

HPV (Human Papilloma Virus), CIN (Cervical Intraepithelial Neoplasia), Q (Quercetin), Su (Sulphoraphane), Sc (Scopoletin), In (InUa), Ic (Icarin), H (High), L (Low), UAE (Ultrasonic-Assisted Extraction), ME (Maceration Extraction),HE/He-Hela,Si-Siha,Stnd-Standard,MTX-Methotrexate

.

6.ETHICS APPROVAL

Application to be submitted to the CPCSEA, New Delhi after approval of Institutional Animal Ethics Committee (IAEC).Form B (per rule 8(a)* for Submission of Research Protocol (s).Application No.: RKCP/COl/Re/22/125,Application for Permission for Animal Experiments.Application to be submitted to the CPCSEA, New Delhi after approval of Institutional Animal Ethics Committee (IAEC)

7.CONSENT TO PARTICIPATE

N/A

8.CONSENT FOR PUBLICATION

This manuscript does not contain any individual person's data in any form (including images, videos, or case reports). Therefore, **not applicable**.

9.FUNDING

Not applicable.

.

REFERENCE

1. World Health Organization. (2023). Cervical cancer: Key facts. World Health Organization.
2. Schiffman, M., & Castle, P. E. (2005). The promise of global cervical cancer prevention. The New England Journal of Medicine, 353(20), 2101–2104. https://doi.org/10.1056/NEJMp058171
3. Hanahan, D., & Weinberg, R. A. (2011). Hallmarks of cancer: The next generation. Cell, 144(5), 646–674. https://doi.org/10.1016/j.cell.2011.02.013
4. Monk, B. J., Tewari, K. S., & Koh, W. J. (2007). Multimodality therapy for locally advanced cervical carcinoma. Journal of Clinical Oncology, 25(20), 2952–2965. https://doi.org/10.1200/JCO.2007.10.8328
5. Kelloff, G. J., Crowell, J. A., Steele, V. E., et al. (2004). Progress in cancer chemoprevention. Nature Reviews Cancer, 4(11), 876–888. https://doi.org/10.1038/nrc1474
6. Riss, T. L., Moravec, R. A., Niles, A. L., et al. (2016). Cell viability assays. In Assay guidance manual. National Institutes of Health.
7. Galluzzi, L., Vitale, I., Aaronson, S. A., et al. (2018). Molecular mechanisms of cell death. Cell Death & Differentiation, 25(3), 486–541. https://doi.org/10.1038/s41418-017-0012-4
8. Crowley, L. C., Marfell, B. J., Scott, A. P., & Waterhouse, N. J. (2016). Measuring cell death by propidium iodide uptake. Cold Spring Harbor Protocols, 2016(7). https://doi.org/10.1101/pdb.prot087163
9. Elmore, S. (2007). Apoptosis: A review of

programmed cell death. Toxicologic Pathology, 35(4), 495–516. https://doi.org/10.1080/01926230701320337

10. Kroemer, G., Galluzzi, L., Vandenabeele, P., et al. (2009). Classification of cell death: Recommendations of the NCCD. Cell Death & Differentiation, 16(1), 3–11. https://doi.org/10.1038/cdd.2008.150

11. Mosmann, T. (1983). Rapid colorimetric assay for cellular growth and survival. Journal of Immunological Methods, 65(1–2), 55–63. https://doi.org/10.1016/0022-1759(83)90303-4

12. Berridge, M. V., & Tan, A. S. (1993). Characterization of cellular reduction of MTT. Archives of Biochemistry and Biophysics, 303(2), 474–482. https://doi.org/10.1006/abbi.1993.1311

13. Cory, A. H., Owen, T. C., Barltrop, J. A., & Cory, J. G. (1991). Use of soluble tetrazolium assays. Cancer Communications, 3, 207–212.

14. Sackmann, E. K., Fulton, A. L., & Beebe, D. J. (2014). The present and future role of microfluidics. Nature, 507(7491), 181–189. https://doi.org/10.1038/nature13118

15. Zhang, B., & Radisic, M. (2017). Organ-on-a-chip devices. Lab on a Chip, 17(14), 2395–2420. https://doi.org/10.1039/C7LC00230A

16. Polacheck, W. J., Zervantonakis, I. K., & Kamm, R. D. (2013). Tumor cell migration in complex microenvironments. Nature Reviews Cancer, 13(5), 365–379. https://doi.org/10.1038/nrc3495

17. Arnaoutova, I., & Kleinman, H. K. (2010). In vitro angiogenesis assays. Nature Protocols, 5(4), 628–635. https://doi.org/10.1038/nprot.2010.6

18. Carmeliet, P., & Jain, R. K. (2011). Molecular mechanisms of angiogenesis. Nature, 473(7347), 298–307. https://doi.org/10.1038/nature10144

19. Greco, W. R., Bravo, G., & Parsons, J. C. (1995). The search for synergy. Cancer Research, 55(23), 5665–5673.

20. van der Worp, H. B., Howells, D. W., Sena, E. S., et al. (2010). Can animal models improve translation? Nature Reviews Drug Discovery, 9(10), 790–800. https://doi.org/10.1038/nrd3285

21. Galluzzi, L., Bravo-San Pedro, J. M., Vitale, I., et al. (2015). Essential versus accessory aspects of cell death. Cell Death & Differentiation, 22(1), 58–73. https://doi.org/10.1038/cdd.2014.137

22. Kerr, J. F. R., Wyllie, A. H., & Currie, A. R. (1972). Apoptosis: A basic biological phenomenon. British Journal of Cancer, 26(4), 239–257. https://doi.org/10.1038/bjc.1972.33

23. Leist, M., & Jäättelä, M. (2001). Caspase-independent cell death. Nature Reviews Molecular Cell Biology, 2(8), 589–598. https://doi.org/10.1038/35085008

24. Riss, T. L., Niles, A. L., Moravec, R. A., et al. (2019). Cytotoxicity assays. Methods in Molecular Biology, 1601, 87–111. https://doi.org/10.1007/978-1-4939-6960-9_7

25. Hengartner, M. O. (2000). The biochemistry of apoptosis. Nature, 407(6805), 770–776. https://doi.org/10.1038/35037710

26. Masters, J. R. (2002). HeLa cells 50 years on. Nature Reviews Cancer, 2(4), 315–319. https://doi.org/10.1038/nrc775

27. Freshney, R. I. (2015). Culture of animal cells: A manual of basic technique and specialized applications (7th ed.). Wiley-Blackwell.

28. Strober, W. (2015). Trypan blue exclusion test. Current Protocols in Immunology, 111(1). https://doi.org/10.1002/0471142735.ima03bs111

29. Altman, F. P. (1976). Tetrazolium salts and formazans. Progress in Histochemistry and Cytochemistry, 9, 1–56.

30. Stockert, J. C., Horobin, R. W., Colombo, L. L., & Blázquez-Castro, A. (2018). Tetrazolium salts in cell biology. Acta Histochemica, 120(3), 159–167. https://doi.org/10.1016/j.acthis.2018.02.005

31. Berridge, M. V., Herst, P. M., & Tan, A. S. (2005). Tetrazolium dyes in cell biology. Biotechnology Annual Review, 11, 127–152. https://doi.org/10.1016/S1387-2656(05)11004-7

32. Denizot, F., & Lang, R. (1986). Rapid colorimetric assay improvements. Journal of Immunological Methods, 89(2), 271–277. https://doi.org/10.1016/0022-1759(86)90368-6

33. Fotakis, G., & Timbrell, J. A. (2006). In vitro cytotoxicity assays comparison. Toxicology Letters, 160(2), 171–177. https://doi.org/10.1016/j.toxlet.2005.07.001

34. McAfee, A. J., McSorley, E. M., Cuskelly, G. J., et al. (2010). Red meat consumption and cancer risk. Meat Science, 84(1), 1–13.

35. Williams, P. G. (2007). Nutritional composition of red meat. Nutrition & Dietetics, 64(S4), S113–S119.

36. Ruxton, C. H. S., Reed, S. C., Simpson, M. J. A., & Millington, K. J. (2004). Omega-3 fatty acids. Journal of Human Nutrition and Dietetics, 17(5), 449–459.

37. Workman, P., Aboagye, E. O., Balkwill, F., et al. (2010). Guidelines for animal research. British Journal of Cancer, 102(11), 1555–1577.

38. Shojaei, F. (2012). Anti-angiogenesis therapy in cancer. Cancer Letters, 320(2), 130–137.

39. Jayson, G. C., Kerbel, R., Ellis, L. M., & Harris, A. L. (2016). Anti-angiogenic therapy in oncology. The Lancet, 388, 518–529.

40. Bishop, E. T., Bell, G. T., Bloor, S., et al. (1999). In vitro angiogenesis models. Angiogenesis, 3, 335–344.

41. Donovan, D., Brown, N. J., Bishop, E. T., &

Lewis, C. E. (2001). Comparison of angiogenesis assays. Angiogenesis, 4, 113–121.

42. Auerbach, R., Lewis, R., Shinners, B., Kubai, L., & Akhtar, N. (2003). Angiogenesis assays overview. Clinical Chemistry, 49, 32–40.

43. Polacheck, W. J., Charest, J. L., & Kamm, R. D. (2011). Interstitial flow influences cell migration. Proceedings of the National Academy of Sciences, 108(27), 11115–11120.

44. Sobrino, A., Phan, D. T. T., Datta, R., et al. (2016). 3D microtumors with perfused vasculature. Scientific Reports, 6, 31589.

45. Zink, D., Fischer, A. H., & Nickerson, J. A. (2004). Nuclear structure in cancer. Nature Reviews Cancer, 4(9), 677–687.

46. Dahl, K. N., Ribeiro, A. J. S., & Lammerding, J. (2008). Nuclear mechanics. Circulation Research, 102(11), 1307–1318.

47. Polacheck, W. J., Kutys, M. L., Yang, J., et al. (2017). Vascular barrier regulation. Nature, 552(7684), 258–262.

48. Pollard, T. D., & Cooper, J. A. (2009). Actin and cell movement. Science, 326(5957), 1208–1212.

49. Karar, J., & Maity, A. (2011). PI3K/AKT/mTOR signaling in angiogenesis. Frontiers in Molecular Neuroscience, 4, 51.

50. Johnson, I., & Spence, M. T. Z. (2010). The molecular probes handbook (11th ed.). Life Technologies.

51. Wulf, E., Deboben, A., Bautz, F. A., Faulstich, H., & Wieland, T. (1979). Fluorescent phallotoxin labeling. Proceedings of the National Academy of Sciences, 76(9.), 4498–4502.

52. Schneider, C. A., Rasband, W. S., & Eliceiri, K. W. (2012). NIH ImageJ. Nature Methods, 9(7), 671–675.

53. Zudaire, E., Gambardella, L., Kurcz, C., & Vermeren, S. (2011). Quantitative vascular analysis tool. PLoS ONE, 6(11), e27385.

54. Folkman, J. (2007). Angiogenesis and drug discovery. Nature Reviews Drug Discovery, 6, 273–286.

55. Ferrara, N. (2004). Vascular endothelial growth factor. Endocrine Reviews, 25, 581–611.

56. Kilkenny, C., Browne, W. J., Cuthill, I. C., Emerson, M., & Altman, D. G. (2010). ARRIVE guidelines. PLoS Biology, 8, e1000412.

57. Waggoner, S. E. (2003). Cervical cancer. The Lancet, 361, 2217–2225.

58. Bhatla, N., Aoki, D., Sharma, D. N., & Sankaranarayanan, R. (2018). Cervical cancer overview. International Journal of Gynecology & Obstetrics, 143, 22–36.

59. Cory, J. G., Carter, G. L., & Bacus, S. S. (1991). Drug sensitivity assays. Cancer Letters, 57, 101–110.

60. Scudiero, D. A., Shoemaker, R. H., Paull, K. D., et al. (1988). Drug sensitivity screening. Cancer Research, 48, 4827–4833.

61. McCaffrey, L. M., & Macara, I. G. (2011). Epithelial organization and polarity. Nature Reviews Molecular Cell Biology, 12, 45–54.

62. Staton, C. A., Reed, M. W. R., & Brown, N. J. (2009). Angiogenesis assays. International Journal of Experimental Pathology, 90(3), 195–221.

63. Carmeliet, P. (2005). Angiogenesis in cancer. Nature Medicine, 11(5), 540–544..